



**UNIVERSITÀ DEGLI STUDI DI PADOVA**  
DIPARTIMENTO DI INGEGNERIA INDUSTRIALE  
CORSO DI LAUREA MAGISTRALE IN INGEGNERIA DEI MATERIALI

**Tesi di Laurea Magistrale in Ingegneria dei Materiali**

**SYNTHESIS, CHARACTERIZATION AND  
MAGNETO-RHEOLOGICAL PROPERTIES OF  
BIOPOLYMER BASED  
MAGNETOSENSITIVE NANOCOMPOSITES**

*Relatore: Prof. Giovanna Brusatin*  
*Correlatore: Prof. Fayna Mammeri*

*Laureanda: Giulia Franceschin*  
*Matricola: 1035082*

ANNO ACCADEMICO 2013 – 2014



# Acknowledgement

Firstly I would like to thank my supervisors Giovanna Brusatin and Fayna Mammeri that gave me the opportunity to follow this project and to experience a wonderful period in Paris Diderot University.

I'm especially grateful to Fayna Mammeri for her support, to have shared her desk during my internship in Paris and for the funny stories she used to tell.

I thank Ammar Souad, Laurence Ourry and all the guys of 8<sup>th</sup> floor laboratory for their aid during my first synthesis experiences, Francois Chau who helped me in the grafting operations with fluoresceine and Jean-Yves Piquemal to have introduced me to UV-Vis analysis.

Furthermore I would like to thank the research team of physics departments of Paris University for the rheological investigations, among which Alain Ponton and Florent Carn from MSC laboratory and Philippe Djemia from Paris 13 University.

In a particular way, I would like to thank my colleagues and friends Damien Braccagni, who worked with me to the project since my very first days in the laboratory and introduced me in the rheological studies, and Jean-Luc Mutabazi, who helped me to synthesize a huge nanoparticles amount, for the nice lunches and moments we spent together outside the lab too.

Moreover, I thank my Italian companions Sofia Marchesini and Mattia Pasut that constantly shared experiences with me during these six months.

Last but not least I'm grateful to all friends of mine, Valentino, the Lidl and in particular my family that always support me in my choices and that helped me during my whole university life.



# Abstract

In this work, the development of a novel magnetic sensitive biopolymer-based nanocomposite is investigated.

First, magnetic iron oxide nanoparticles (NPs) were synthesized by the polyol method, in order to obtain particles with average diameter of 10nm, and then functionalised by grafting bifunctional ligands for establishing electrostatic bonds between both the alginate chains of the biopolymer, used as matrix, and a fluorophore molecule, employed to mimic drugs.

It was chosen to graft three different organic ligands, all presenting an ammine function on one side, for the coupling with the matrix and with the fluorophore, and at least a hydroxyl function on the other, for the linking to NPs surface.

The NPs produced in this way were characterised by transmission electron microscopy (TEM), X-ray diffraction (XRD), infra-red spectroscopy FT-IR with ATR (Attenuated Total Reflectance) accessory and thermogravimetric analysis (TGA); moreover, zeta potential analysis permitted to investigate the variation of NPs stability in relation to both the pH of the environment and the ligand grafted onto NP.

UV-Visible spectroscopy was used to verify the linking of the drug mimetic fluorophore to NPs' surface and to study the attachment stability in time, simulating ageing by consecutive rinsing of grafted NPs.

Finally, a composite, made up of alginate biopolymer matrix containing magnetic iron oxide functionalised NPs, was assembled and observed from a rheological point of view, after the application of a magnetic field.



# Contents

<b>Introduction .....</b>	<b>1</b>
<b>Applications.....</b>	<b>5</b>
1.1 Development of materials for drug delivery.....	5
1.1.1 State of the art .....	5
1.1.2 Presentation of the project and previous results.....	7
<b>Experimental Procedure and Materials .....</b>	<b>9</b>
2.1 Iron Oxide Nanoparticles .....	9
2.1.1 Presentation .....	9
2.1.2 Synthesis of maghemite nanoparticles .....	12
2.2 Maghemite NPs surface functionalization.....	16
2.2.1 Introduction .....	16
2.2.2 The dopamine.....	16
2.2.3 The amino-silane .....	18
2.2.4 The amino-phosphonic acid .....	20
2.3 Fluorophore grafting for drug mimicry .....	21
2.3.1 Introduction .....	21
2.3.2 FITC labelling protocol.....	22
2.3.3 Experimental procedure adopted for FITC labelling .....	22
2.3.4 FITC labelled NPs' ageing experimental process .....	24
2.4 Biopolymer-based nanocomposite preparation .....	24
2.4.1 Introduction .....	24
2.4.2 The alginates as biopolymer matrix .....	25
2.4.3 Experimental procedure for alginate-based nanocomposite preparation .....	28
<b>Characterisation Methods .....</b>	<b>30</b>
3.1 Bare and decorated nanoparticles .....	30
3.1.1 Infra-Red spectroscopy .....	30
3.1.2 X-Ray diffraction (XRD) .....	32
3.1.3 Transmission Electron Microscopy (TEM) .....	35
3.1.4 Thermo-Gravimetric Analysis (TGA).....	36
3.1.5 Zeta potential measurements.....	38
3.1.6 SQUID for magnetic measurements .....	41
3.2 FITC labelled nanoparticles .....	42
3.2.1 Ultraviolet-visible (UV-Vis) spectroscopy .....	42
3.3 Alginate-based nanocomposites.....	46

3.3.1 Rheological basic concepts .....	46
3.3.2 Magneto-rheological investigation: experimental conditions.....	52
3.3.3 Optical microscopy under magnetic field.....	55
<b>Characterisation Results.....</b>	<b>56</b>
4. 1 Bare maghemite nanoparticles .....	56
4.1.1 IR-ATR spectroscopy .....	56
4.1.2 X-Ray Diffraction .....	57
4.1.3 Transmission Electron Microscopy .....	58
4.1.4 Thermo Gravimetric Analysis .....	60
4.1.5 SQUID magnetic measurements.....	61
4.2 Decorated nanoparticles .....	62
4.2.1 IR-ATR Spectroscopy.....	62
4.2.2 Thermo Gravimetric Analysis .....	65
4.2.3 Stability valuation by Zeta Potential analysis.....	68
4.3 FITC labelled nanoparticles .....	70
4.3.1 UV-Vis spectroscopy .....	70
4.3.2 Calculation of FITC grafted amount.....	73
4.4 Alginate-based nanocomposites .....	74
4.4.1 Oscillatory measurements.....	74
4.4.2 Shear measurements .....	76
4.4.3 Magnetic reversibility measurements .....	76
4.4.4 Optical microscopy under magnetic field.....	77
<b>Future Developments .....</b>	<b>79</b>
5.1 Functional groups for NPs grafting.....	79
5.2 Rheological analysis.....	80
<b>Conclusion.....</b>	<b>83</b>
<b>Nomenclature.....</b>	<b>87</b>
<b>Bibliography .....</b>	<b>89</b>



# Introduction

Due to their unique physical properties and their ability to operate at the cellular and molecular level of biological interactions, magnetic nanoparticles (MNPs) have been actively investigated as the next generation of targeted delivery for more than 30 years<sup>1,2,3</sup>. The success of target delivery and therapy is based on a direct transportation of the bioactive compound to the centre of the body in order to avoid side-effects. The use of magnetic materials depends on their properties, including magnetization, morphology, shape, size, and polydispersity.

Among the main well-known methods developed for MNPs synthesis, we can mention aqueous precipitation, sol-gel synthesis, polyol process, microemulsion route, sonochemical reaction, hydrothermal reaction, thermal decomposition, electrospray synthesis and laser pyrolysis<sup>4,5,6,7,8,9</sup>. It is established that the synthesis conditions affect directly the magnetic properties of these particles<sup>10,11,12</sup>.

Plenty of these materials are coupled to different carriers like polymers, liposomes, micelles, which result in systems with multifunctional capabilities for drug delivery, biocatalysis, targeted infection, magnetic resonance imaging, sensing, etc. The resulting nanostructures are in clinical trials; nevertheless, up to now, few of them have reached the market.

The control of the surface chemistry of MNPs is required to avoid the aggregation due to their large surface-to-volume ratio and dipole-dipole interactions and to provide them biocompatibility, nonspecific adsorption to cells and bioconjugation properties. Indeed, large agglomerates limit their diffusion into the human body. Several approaches of modification of the surface of MNPs with small molecules including biomolecules have been investigated, the most general being the post-addition of water-soluble ligands.

Polymers bearing at least two different functional groups able to bind to magnetic particle surface can enhance colloidal stability of inorganic nanoparticles, including MNPs, and provide mechanical and chemical stability to nanomaterials. Hybrid polymer-decorated MNPs embedded in cross-linked gels matrixes also enable the encapsulation of therapeutic and imaging agents for targeted delivery systems. Consequently, polymeric matrixes ensure the dispersion of the MNPs, enhance their stability (sedimentation, shielding), chemical functionality, compatibility (hydrophobicity or hydrophilicity, toxicity, stealth), and biocompatibility.

In this context, useful engineering of MNPs for target delivery systems of therapeutic agents has grown as a result of the increasing demand for delivery systems able to protect, transport, and selectively deposit therapeutic agents to desired sites. The obvious

advantage of using superparamagnetic polymer based composites for the delivery of biocompounds is that the system can be easily localized using an external magnetic field, imaged by MRI and finally, the release may be achieved in a controlled manner.

The following study is focused on the design of nanometer sized novel drug-loaded polymer based magnetic architectures, consisting in multi magnetic cores embedded simultaneously in a biopolymeric matrix to form *nanocomposites*. Indeed, it is still a challenge to develop a method for immobilizing a biosubstance, like a drug or a chromophore, between the polymer chains on a magnetic carrier, and to deliver them under external and controlled magnetic stimuli, able for instance to induce a local temperature increase or a rheological behaviour change.

These bioproduct-loaded materials exhibit several advantages:

- The small particle size allows a large diffusion into the blood pool;
- Their high surface area favours the fixation of a great number of bioactive molecules;
- The biocompatibility of the desired hybrid or composite architectures makes them safe.
- Due to their magnetic properties, they can be headed to the right site with external magnets; thus, smaller dose is required and fewer side effects are produced.
- Besides heading to the target site, the drug can be delivered specifically there thanks to external controlled magnetic stimuli (hyperthermia effect, magnetorheological effect, etc.) that produce changes in the polymeric chains conformation or reticulation.

The purpose here is to couple MNPs directly to hydrophilic polymer chains through covalent or ionic interactions. In these cases, bifunctional ligands are required since they have to be anchored simultaneously to the surface of the particle and to the polymer chains.

The present work is part of a wider project started since 2011 in ITODYS laboratory (Paris Diderot University), aiming at analysing and solving the design of nanometer sized novel drug-loaded polymer-based magnetic architectures, from physical, chemical and biochemical point of view.

In particular, the proposal is to continue and connect previous works carried out by both L. Ourry during her master thesis <sup>6</sup>, about synthesis and characterisation of iron oxide NPs with functionalised surface, and the MSC laboratory of Paris Diderot University, about investigation on rheological properties of bionanocomposites obtained by coupling functionalised iron oxide NPs with a biopolymer matrix of alginate.

Specific objectives of this thesis are divided into three main parts, which are:

- Improvement of colloidal stability of magnetic NPs at physiological pH by decoration of their surface with different kinds of ligands, in order to avoid aggregation due to the high surface-to-volume ratio of NPs;
- Effectiveness of such decorated NPs in anchoring organic fluorophore molecules, that are used to mimic drugs' behaviour;
- Obtention of a bio-nanocomposite, assembling decorated NPs with the solution of alginate, and to study its rheological properties after the application of a magnetic field.

In the first chapter, the state of art of drug delivery systems will be presented, as far as focusing especially on magnetic biocompatible nanocomposite; the results obtained in the former part of the project by ITODYS and MSC laboratories will be also exposed in this framework.

The second chapter will investigate the materials and methods adopted during this work, such as the nature of the synthesized NPs, with the presentation of the maghemite iron oxide, the nature of bi-functional molecules chosen to decorate NPs surface as long as their grafting techniques, the *mimic drug* technique used to estimate the efficiency in trapping drugs molecules of each decorated NPs type, and the composition of the hybrid material from an alginate solution mixed up with maghemite NPs.

The third chapter will focus on various characterization methods used during the experience for each synthesized materials, i.e. bare and decorated NPs, fluorophore-labelled NPs and bio-composite nano-charged material.

The results of such characterizations will be discussed in the fourth chapter, with particular attention to zeta potential results, which allow investigating about NPs colloidal stability in relation to the pH of the NP solution; in other words, zeta potential characterisation will let reach the first one of the purposed objective, comparing the different behaviour of decorated maghemite depending on the specific functional molecule grafted onto the surface. Particular attention will be devoted also to mimetic drug-loaded NPs characterization by UV-Vis spectroscopy and hybrid materials characterization, carried out by mean of novel magnetic and magneto-rheological tests, achieved in MSC laboratory.

Finally, in the fifth chapter, the possible future developments of the project will be suggested.



# Chapter 1

## Applications

### 1.1 Development of materials for drug delivery

Inside this section the scenario regarding materials applied for drug delivery will be presented, in order to focalize the role of magnetic bio-nano-composite materials.

Therefore, previous results obtained in ITODYS and MSC laboratories will be briefly exposed, so as to better understand the work sets out hereunder.

#### *1.1.1 State of the art*

Controlling and driving the drugs release inside the human body has been investigating since a long time, thanks to the high relevance it has in biological, medical and pharmaceutical applications; indeed, certain drugs rarely achieve their maximum therapeutic action through conventional injection techniques, so that in a typical injection a greater dosage than necessary must be administered to keep the drug concentration within the effective therapeutic margin, leading to subsequent broader side effects.

Already in the early '70, studies about drugs delivery systems were conducted according to the available knowledge of the time. For examples, Zaffaroni<sup>13</sup> succeeded in releasing drugs in a controlled rate for a prolonged time, dispersing molecules of drug in a solid matrix material and surrounding it by an outer polymeric membrane; in this case the release was controlled by the slowness of drugs in passing through the polymeric membrane, so it was governed only by a kinetic factor and it didn't afford to direct the route a priori.

Some years later, colloidal particles as microspheres, microcapsules or emulsions, made of polymeric materials, had been proposed as a mean of directing drugs contained therein to specific sites in the body. This concept, also known as drug targeting, had been well described in a number of publications, review articles and books.

Among these, the use of polymeric microsphere systems as vehicles for delivering drugs by a variety of routes was considered<sup>14</sup>. Microsphere formulation was discussed with emphasis on the role of surface properties and how these could determine the fate of administered particles.

In recent years, significant effort has been devoted to develop nanotechnology for drug delivery, as it offers a suitable mean of delivering small molecular weight drugs, as well as macromolecules such as proteins, peptides or genes by either localized or targeted delivery to the tissue of interest. In particular, one of the most important domains of this investigation involves the realization of nanocomposite materials, based on biopolymer matrices in relation to reasons of biocompatibility, already exposed inside the Introduction. Pharmaceutical nanotechnology focuses on formulating therapeutically active agents in nanoforms such as nanoparticles, nanocapsules, micellar systems and conjugates, whose nanometer size-ranges offer certain distinct advantages for the process of drug release. First, nano-structures can penetrate deep into tissues through fine capillaries, cross the fenestration present in the epithelial lining, and are generally taken up efficiently by the cells; this allows efficient delivery of therapeutic agents to target sites in the body, such as the lung, liver, bone marrow. Then, by modulating polymer characteristics, one can control the release of a therapeutic agent from NPs to achieve desired therapeutic level in target tissue for required duration for optimal therapeutic efficacy.

**Table 1.1.** *Examples of bio-applications of polysaccharide based nanocomposites.*

Applications		Reinforcement   Matrix	References
Biotechnology	Bioseparation	Fe <sub>3</sub> O <sub>4</sub>   Dextran Fe <sub>3</sub> O <sub>4</sub>   Gum arabic Fe <sub>3</sub> O <sub>4</sub>   Chitosan	Heebol-Nielsen et al., 2004 Batalha et al., 2010 Liu et al., 2009
	Biolabeling Biosensing	Au, Ag   Chitosan Au, Ag   Alginate QDs   Chitosan	Santos Jr. et al., 2004; Wei et al., 2009 Lim et al., 2010; Saha et al., 2009 Tan et Zhang, 2005
	Antimicrobial	Ag   Chitosan Ag   Hyaluronan	Potara et al., 2001; Travan et al., 2009 Kemp et al., 2009
Biomedical	Clinical imaging	Fe <sub>3</sub> O <sub>4</sub>   Dextran	Chachuat et al., 1995; Corot et al., 2006
	Drug delivery	Fe <sub>3</sub> O <sub>4</sub>   Alginate Fe <sub>3</sub> O <sub>4</sub>   Chitosan Fe <sub>3</sub> O <sub>4</sub>   Heparin	Brulé et al., 2011 Hu et al., 2007 Khurshid et al., 2009
	Cancer hyperthermia	Fe <sub>3</sub> O <sub>4</sub>   Chitosan Fe <sub>3</sub> O <sub>4</sub>   Pullulan acetate	Zhao et al., 2009 Gao et al., 2010

Among the large number of available polymers to produce such bio-nano-composites, the use of polysaccharides, derived from natural sources, achieved more interest in the contest

of bioapplications. Some of the most representative examples and applications of polysaccharides based nanocomposites, from literature, are listed in Table 1.1<sup>15</sup>.

On the other hand, as it can be seen in this table, composite materials are always coupled with specific inorganic nanofillers, which allow a further engineering of the delivery system. Magnetic NPs have been actively investigated, as the next generation of targeted delivery for more than 30 years<sup>1,2,3</sup>, according to their properties, like magnetization, morphology, shape, size and polydispersity.

Organic polymers and inorganic NPs give possibility to form self-assembled supramolecular morphologies, with great potential for novel hydrogel polymer based nanocomposites elaboration, which can be used for various biomedical applications. Indeed, ever-growing hydrogel technology<sup>16</sup> has led to surprising advances in pharmaceutical and biomedical era<sup>17-20</sup>.

By definition, hydrogels are polymeric networks with three-dimensional configuration capable of imbibing high amounts of water or biological fluids<sup>21-23</sup>, according to hydrophilic groups, such as  $-OH$ ,  $-CONH-$  and  $-CONH_2-$ , in polymers forming structures. Due to the presence of these groups and domains in network, these structures have some common physical properties resembling that of the living tissues, than any other class of synthetic biomaterials, which are their high water content, their soft and rubbery consistency, and low interfacial tension with water or biological fluids.

For example, amine functionalised iron oxide NPs were obtained using an effective process to coat NPs with amine terminated PEG molecules<sup>24</sup>; such a hybrid was found to be water soluble with long-term stability in biological media and revealed itself a promising medical technology based on magnetic particle imaging (MPI).

Also amine-functionalised silica NPs were found to be a gene delivery platform for both in vitro and in vivo applications<sup>25</sup>; amine terminated TEG functionalized mesoporous silica NPs transported DNA and chemicals into plant cells and intact leaves<sup>26</sup>.

### *1.1.2 Presentation of the project and previous results*

The present study aims at synthesizing alginate-based hydrogels, in which NPs are then introduced.

In this context, among various polymer materials, alginate attracted attention, since this polysaccharide is characterised by carboxylic functionalities that can be easily deprotonated in water at neutral pH and form an anionic polyelectrolyte, bearing carboxylate groups. This feature can be applied in coupling alginate with NPs through positively charged groups, grafted on NPs' surface, sensible to Coulomb attraction with carboxylate groups of the polymer.

NPs may extend hydrogel application field, thanks to their specific physical properties, besides enhancing its mechanical properties and its rigidity. In the specific case, iron oxide NPs were chosen for their magnetic properties, since their suspension into polymer matrix allow controlling its position by application of a static magnetic field. This same property permit also to heat the hydrogel, by means of an alternated magnetic field that act changing the network conformation and thereby his capability in retaining drug's molecules.

The connections between filler and matrix have an important role, directly linked to final rheological properties of the whole system; the possibility to enhance this connection regards NPs' decoration with desired ligands on their surface.

In the first part of this project, L. Ourry's study <sup>27</sup> focalized on NPs' grafting of amine ( $\text{NH}_2/\text{NH}_3^+$ ) functionalities, by two different kinds of molecules: dopamine (DOPA) and aminopropyltriethoxysilane (APTES); the functionalised NPs were then introduced into an alginate solution and into a gel of the same polymer, in order to analyse system's behaviour under magnetic stimulus.

For both the systems with DOPA and APTES in solution, an increase of *viscosity* and an inversion of *elastic* ( $G'$ ) and *viscous* ( $G''$ ) *modulus* values were observed after application of a continuous magnetic field, that implies a viscoelastic properties modification of the system: it behaves as a solution, that is  $G'' > G'$ , without the magnetic field and as a gel, with  $G' > G''$ , under magnetic field.

On another hand, analysis of the system gel with APTES NPs highlighted a delay of *gelification time* in comparison with the ordinary time measured without NPs.

C. Galindo Gonzalez took up other rheological measures, upon the same system with APTES NPs in alginate solution, during her post-doctoral stay in MSC laboratory at Paris Diderot University. She observed a reversible enhancement of both *elastic* (or *storage*) and *viscous* (or *loss*) *modulus* at low *shear rate* and she explained this by intramolecular electrostatic interaction between the positively charged  $-\text{NH}_3^+$  groups at the NPs surface and the negatively charged carboxylate  $-\text{COO}^-$  of sodium alginate chains; this last assumption is supported by microscopic observation showing magnetic-induced structures inside the nanocomposite.

This study aimed at studying the stability of different NPs in suspension, but also at studying the rheological properties of the system made from alginate and DOPA decorated NPs, since dopamine grafting on surface is easier than the APTES's one. Other reasons for considering dopamine as decorating ligand will be explained by the characterization results of grafted NPs.



# Chapter 2

## Experimental Procedure and Materials

### 2.1 Iron Oxide Nanoparticles

#### 2.1.1 Presentation

The iron oxide is an iron and oxygen based compound, often found in a sub-micrometric size form, like powder.

Many types of iron oxides exist in nature or by synthesis, each exhibiting different properties such as colour, shapes, magnetic skills. Some of these types found naturally are:

- *Iron oxide (II)*,  $FeO$  also called *wustite*;
- *Iron oxide (II, III)*,  $Fe_3O_4$  or *magnetite*;
- *Iron oxide (III)*,  $Fe_2O_3$  that can be found in its turn in four different mineral phases; one of these,  $\gamma\text{-}Fe_2O_3$  *maghemite* is a brown powder and it is the one with the most interesting feature for this project.

Biomedical applications require biocompatible, magnetic and interacting NPs, as already seen; maghemite and magnetite well fulfil the first and second one requirement, while NP surface functionalization seems to be a suitable solution for the third one.

Iron oxide embedding in a matrix is often explained by a small-scale special property shown by NPs from a certain size on and smaller, that is *superparamagnetism*. The choice for maghemite, whereas, is derived from its greater grafting simplicity. Indeed, magnetite and maghemite exhibit very similar magnetic properties (saturation magnetization) but magnetite leads little by little to maghemite by oxidation in presence of air. Hence, maghemite is more stable.

##### 2.1.1.1 Magnetic behaviours and the superparamagnetism

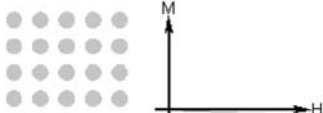
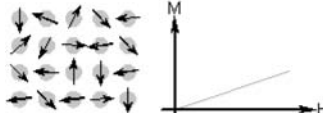
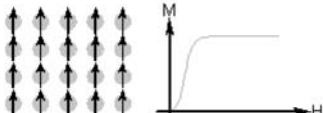
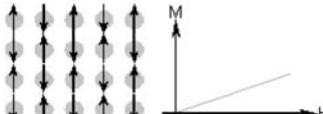
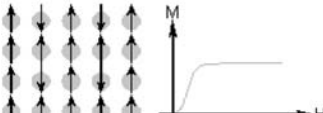
The origin of magnetism in matter lies in the orbital and spin motions of electrons and how the electrons interact with one another. Different types of magnetism can be distinguished in relation to how materials respond to an external applied magnetic field, according to the magnetic behaviours classification stated by the Scientific Committee.

Fundamental quantities in magnetic theory are the magnetization  $M$ , that represents the net magnetic dipole moment per unit volume of a certain region of material,  $B$ , that is the magnetic induction and  $H$  that is the magnetizing field; these quantities are related each

other by magnetic susceptibility  $\chi$  and magnetic permeability  $\mu$ , that are respectively the measure of the increase in magnetic moment ( $M$ ) and in magnetic flux ( $B$ ) caused by an applied field ( $H$ ).

The magnetic behaviour of materials can be classified into the major groups in Table 2.1.

**Table 2.1** Classification of the main magnetic behaviours of materials.

Type of magnetism	$\chi$	Magnetic behaviour
<b>Diamagnetism</b>	Small, negative	Atoms have no magnetic moments 
<b>Paramagnetism</b>	Small, positive	Atoms have randomly oriented magnetic moments 
<b>Ferromagnetism</b>	Large, positive, depends on applied magnetic field	Atoms have parallel aligned magnetic moments 
<b>Antiferromagnetism</b>	Small, positive	Atoms have mixed parallel and anti-parallel aligned magnetic moments 
<b>Ferrimagnetism</b>	Large, positive, depends on applied magnetic field	Atoms have anti-parallel aligned magnetic moments 

Ferrimagnetic bulk materials are organised in magnetic domains, separated by Bloch wall when no external magnetic field is applied; inside every single domain, a magnetic resultant is defined in a specific direction. The vector resultant of all the domains' magnetic moments is zero when material is not magnetized.

The material is magnetized approaching an external magnetic field, because magnetic domains with magnetization vector parallel to field direction increase, to the detriment of the others.

Making Bloch wall will require high energetic contribution, if material size is significantly reduced, so that it will prefer to organise itself in magnetic mono-domains.

So each nanoparticle can be considered a mono-domain with a permanent magnetic moment blocked in an easy magnetization direction. In general, this direction is a preferred crystallographic axis, connected to magneto-crystalline anisotropy energy defined in relation (2.1), derived from Stoner-Wohlfarth theory [Stoner 1948]:

$$\Delta E = KV \sin^2 \theta, \quad (2.1)$$

Where  $K$  is the magnetocrystalline anisotropy constant,  $V$  is the NP's volume and  $\theta$  is the angle between magnetization direction and the easy magnetization axis.

When the magnetic moment is aligned with the easy magnetization axis, particle potential energy is minimum.

Particles with volume lower than a critical value have magnetic anisotropy energy comparable to thermal agitation energy (2.2), so that particle monodomain magnetization may change direction spontaneously under temperature influence: this is *superparamagnetism*.

$$E_{th} = K_B T \quad (2.2)$$

Where  $K_B$  is Boltzman constant and  $T$  is the temperature measured in K.

Superparamagnetic materials are characterised by a critical temperature  $T_B$ , under which magnetic anisotropy energy  $\Delta E$  is higher than thermal agitation energy  $E_{th}$ , in such a way that magnetic moments quit swinging from an easy magnetization direction to another: *magnetization* is said to be *blocked*.

$T_B$  depends on NP size and morphology and on the matrix entrapping them; it can range from some 10 to hundreds Kelvin degrees; in the present study, 10nm sized maghemite NPs have  $T_B=250$  K.

#### 2.1.1.2 Maghemite and magnetite crystalline structure

Magnetite is a very common iron oxide, in the form of black powder, with Lewis' formula  $Fe_3O_4$ . Magnetite has a *cubic inverse spinel structure*, where oxygen is placed in face centered cubic sites of the structure, while iron cations fill tetrahedral and octahedral interstitial sites, in the following way:  $(Fe^{3+})_{tetra}[Fe^{2+}Fe^{3+}]_{octa}O_4$  (Figure 2.1.a).

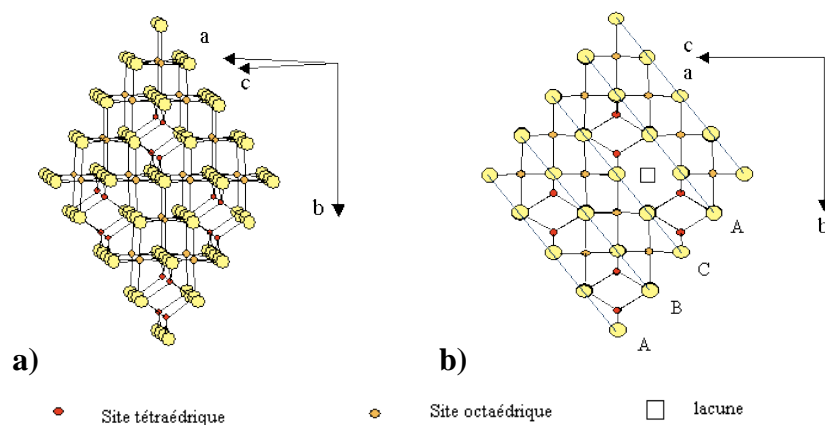


**Figure 2.1** Simplified presentation of magnetite structure (a) and maghemite structure (b).

Maghemite, instead, is a brown powder obtained from magnetite oxidation; indeed, its general formula is  $\gamma-Fe_2O_3$ . The crystalline structure of maghemite is basically the same of

magnetite, in fact maghemite is considered to be like magnetite without  $Fe^{2+}$  adapting itself with cationic vacancies in octahedral site:  $(Fe^{3+})_{tetra} [Fe^{3+}_{5/3} \square_{1/3}]_{octa} O_4$  (Figure 2.1.b).

These iron oxides are both ferrimagnetic at room temperature, as consequence of spinel structure. The superexchange spin interaction between cations filling equivalent sites of the structure is ferromagnetic, while spin interaction between cations in octahedral (in Figure 2.1.b, positions A) and cations in tetrahedral (in Figure 2.1.b, positions B) sites is antiferromagnetic; as a whole, Néel ferromagnetic order is established.

Maghemite surface being oxidized appears to be better than magnetite to graft molecules, thanks to a practical valence variation in favour of ligands complexation.

### 2.1.2 Synthesis of maghemite nanoparticles

Maghemite NPs were synthesized using the *polyol method* in order to have a process control and obtain a size of about 10 nm, with a narrow size distribution.

#### 2.1.2.1 The polyol method

The polyol method is a kind of process based on *soft chemistry* route and used to synthesize inorganic nanoparticles.

At the beginning, F. Fiévet and co.<sup>28</sup> developed it for nanocrystalline powder of transition metals production but, later, it had been employed for metal oxides synthesis<sup>29</sup>.

It consists in hydrolysis of ionic salts in an organic solvent, namely a polyol, and it represents an alternative method to the classic alcoholic sol-gel one. In fact, the polyol solvent is still an alcohol but the precursor is a metal salt, normally a carboxylate or acetate salt instead of an alcoholate. Precursors are basic and they give a strong nucleophilic character to the water.

Forced hydrolysis reactions can be taken inducing metal oxide NPs precipitation, in presence of a controlled amount of water.

Water to metal ions amount ratio must be high enough to permit hydrolysis reaction rather than reduction reaction, but not so high as to stabilize hydroxides instead of oxides. Nevertheless, water addition decrease solution's boiling temperature, whereas it should be high in order to obtain the oxide.

Likewise, the role of the solvent doesn't have to be underestimated. Polyols are polar liquids with a high boiling point, which allow working in a large range of temperature at atmospheric pressure. Their polar character permits to better dissolve metal salts. Various kinds of polyols can be employed as solvent, among which the  $\alpha$ -diols are better reducer than ether glycols (Figure 2.2); so metallic particles are formed more likely in  $\alpha$ -diols

rather than in ether glycols. In polyol synthesis a competition between metal cations reduction and hydrolysis occurs.

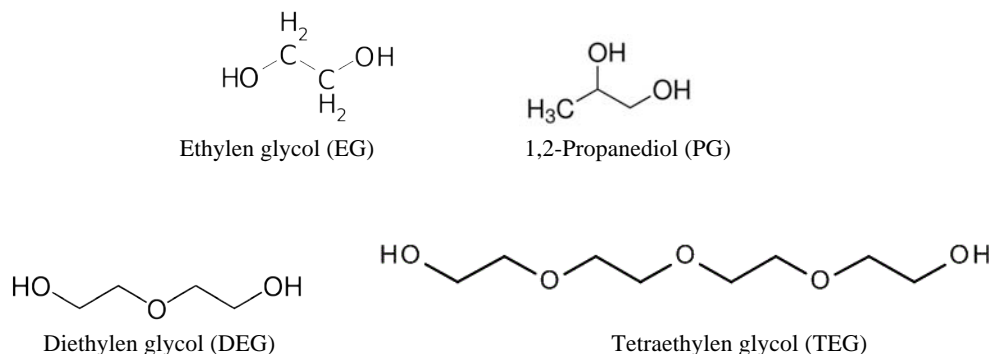


**Figure 2.2** Usual polyols formulas. Ether glycols are upper,  $\alpha$ -diols the lower.

NPs size depends strongly on synthesis temperature. If an isotherm precipitation is supposed to occur, the higher the amount of water, the lower will be the synthesis temperature and smaller the particles.

Other parameters that must be considered are the reaction time and precursor's concentration. About the first one, the longer the heating the bigger is the NPs size. At the same way, the higher the precursor concentration, the larger are the resulting particles.

The reaction mechanism can be described in two steps; during the first one, hydrogen bonds are established between water and acetates. Then, proton is attacked by carbon-oxygen double bond and this can induce the acetate substitution with a  $\text{-OH}$  group.

The formation of bulk solids is always thermodynamically favoured over the formation of small particles with a large surface area, as long as agglomeration of the particles. Therefore, to obtain well-defined characteristics two general conditions must be fulfilled: nucleation and growth must be completely separated and particles coalescence must be prevented.

In metal oxide NPs synthesis, a control of the metallic species concentration allows making monodisperse particles through a control of the growth step, which favours its separation from the nucleation one. Moreover, polyols are able to control particles growth and prevent their agglomeration, coordinating onto NPs' surface. Indeed, among the interesting characteristics of the so-obtained oxide nanoparticles there is their surprisingly good crystallinity that shows also enhanced magnetic characteristics.

In summary, the polyol method offers several advantages: the use of common ionic salts instead of alkoxides, a wide operating temperature range up to boiling point of the polyol, which is higher than the water and alcohol boiling points, and a certain control of the morphological characteristics of the particles.

### 2.1.2.2 Synthesis protocol

A precise amount of iron (II) acetate is dissolved in a solvent consisting of a well know polyol to water volume ratio, by mechanical agitation in a triple-neck round-bottom flask (Figure 2.3.a).

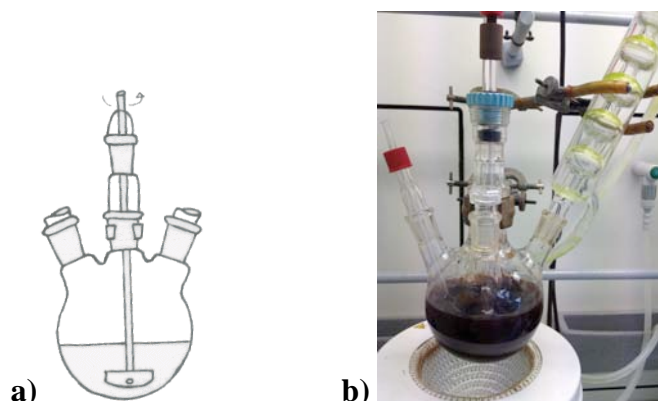


**Figure 2.3** a) Triple-neck round-bottom flask with stirring rod. b) Polyol-mediated synthesis installation

The solution is then lead to the boiling point, while a thermocouple allow to maintain a thermal profile of 6 °C/min during the whole heating process. It is hold under reflux for three hours after boiling begins and finally cooled down to room temperature.

The synthesized powder is magnetic and black in colour, suggesting magnetite  $\text{Fe}_3\text{O}_4$  rather than maghemite  $\text{Fe}_2\text{O}_3$  formation.

Another last step is required for magnetite to maghemite oxidation; particles are washed in boiling water for 10 minutes and then separated from solvent by centrifugation. This operation is repeated four times at least.

After drying in 50°C oven, brown maghemite particles are obtained.

It must be paid attention during oxidation process, since as time goes by maghemite ( $\gamma\text{-Fe}_2\text{O}_3$ ) can also transform itself into hematite ( $\alpha\text{-Fe}_2\text{O}_3$ ). This occurs in two cases: if NPs are dried at high temperature (370-600°C), leading to bigger particles of both maghemite and hematite, and under hydrothermal conditions (150-180°C) leading to bigger particles of only hematite (up to 0,5µm of diameter). In the first case, bigger the maghemite particles are, faster the nucleation and slower the growth occur.

### 2.1.2.3 Experimental working conditions

Synthesis parameters adopted in this study are summarized in Table 2.2 hereunder. Diethyleneglycol (DEG) was employed as solvent. It carries out three different functions: solvent, reducing and complexing agent.

Iron (II) acetate  $\text{Fe}(\text{CH}_3\text{COO})_2$  was the commercial one at 95% by ACROS Organics, DEG  $\text{C}_4\text{H}_{10}\text{O}_3$  at 99% by SIGMA-ALDRICH.

**Table 2.2** Summary of maghemite NPs synthesis conditions.

	m [g]	n [mol]	V [mL]	Tb [°C]	MW [g/mol]	Hydration ratio
<b>Iron (II) acetate</b>	4.03	0.023	-	227	173.93	2.39
<b>Millipore Water</b>	0.001	0.055	1		18.02	
<b>DEG</b>	280	2.64	250		106.12	

Figure 2.3.b depicts the operating system. After the system installation, the mechanic stirrer had been turned on for 5 minutes before actuating heater. Heater was set to arrive up to DEG boiling point (240 °C), with heating profile of 6 °C/min. The boiling point was reached at 227 °C, according to water influence; after 3 hours from when boiling started the heater was turned off.

When solution was cooled at least at 60 °C, about 250mL of acetone were added and the flask was placed upon a magnet at room temperature in order to separate NPs from the supernatant. The amount of acetone doesn't need to be precise, it only has to be about equivalent in volume to the starting solution volume; if separation doesn't occur, it will be necessary to add some other acetone, in order to facilitate it.

After grinding of the dried particles, oxidation had been carried out dispersing it with 2 minutes ultrasounds in 150 mL of Millipore water and boiling the solution for 10 minutes, keeping in stirring. After each washing, particles were separated from the hot supernatant with a magnet and then re-dispersed in fresh water with ultrasounds. This operation had been repeated three times. At the end, maghemite NPs had been dried inside a 60 °C oven over night and obtained as in Figure 2.4.

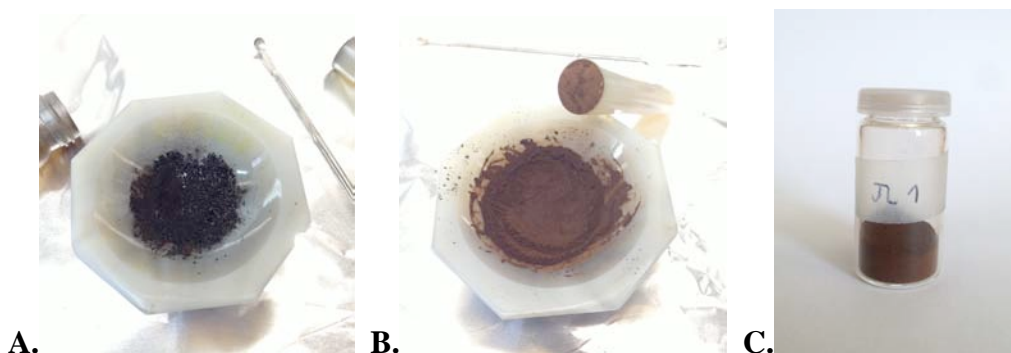


**Figure 2.4** **A.** Maghemite NPs as obtained after oxidation. **B.** Maghemite NPs after crushing in agate mortar. **C.** Finally obtained NPs.

## 2.2 Maghemite NPs surface functionalization

### 2.2.1 Introduction

Tailoring maghemite NPs surface favours several properties; it lead to stable colloidal suspension achievement, to increase the miscibility of nano-objects in organic polymers and to attachment drug molecules onto the surface, too.

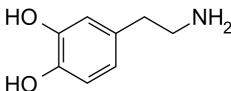
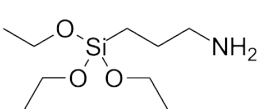
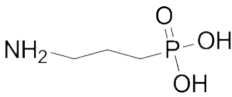
This second step of the work had been 10nm-sized maghemite NPs functionalization, by mean of chemical groups that were able to interact with carboxylate functions of both alginate matrix and fluoresceine later (used to mimic drug behaviour).

The amine  $-NH_2$  functionality was chosen because in physiological pH it is easily protonated to  $-NH_3^+$ , becoming liable to electrostatic interaction with carboxylate groups.

The choice was focused on bifunctional molecules, bearing a group for surface attachment at one side and the amine at the other. The three chosen molecules are:

- Hydroxytyramine hydrochloride or dopamine (DOPA);
- Aminopropyl-triethoxysilane (APTES);
- Aminopropyl-phosphonic acid (PHOS).

*Table 2.3 Structural formulas of grafted molecules.*

DOPA	APTES	PHOSP
		

Molecules nature affects grafting mechanism and also the bond strength between ligand and NP. Different grafting protocols were followed, depending on molecule reactivity with water.

### 2.2.2 The dopamine

Dopamine belongs to catecholamine family, which are neurotransmitters and good chelating agent for  $Fe^{3+}$  ions. Its structural formula is represented in Table 2.3. It uses a  $\sigma$ -donor and a  $\pi$ -donor ligand, realising grafting by mean of complexation reactions with  $Fe^{3+}$  ions on NP's surface: a covalent and an ionic bond are formed. Complexation reaction mechanism is that in Figure 2.5.

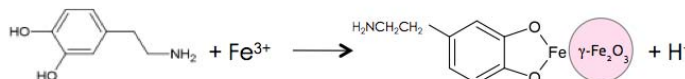


*Figure 2.5 Complexation reaction of  $Fe^{3+}$  ions by catechol derived molecules.*



Dopamine grafting modifies electronic density of  $\text{Fe}^{3+}$  ions placed in octahedral sites of the maghemite structure<sup>30</sup>.

#### 2.2.2.1 Dopamine grafting protocol

The procedure for grafting of dopamine was inspired by H. Blasi work of thesis (2010).

100 mg of NPs are introduced in 100mL of water in a 500mL glass test-tube.

This suspension is placed in ultrasounds bath for 30 minutes, in order to efficiently disperse aggregated NPs.

5 g of dopamine are then added into suspension and the tube is placed again in ultrasounds bath for 45 minutes, during which the reaction in Figure 2.5 is supposed to occur.

As dopamine is soluble in water, an excess of acetone (about 200mL) is added in order to promote hybrids' flocculation; a magnet is placed under the glass tube, attracting particles toward the bottom.

The particles are washed up two other times with the same ratio of water/acetone (1:2) and finally air-dried.

#### 2.2.2.2 Experimental working conditions

The dopamine employed is 3-hydroxytyramide hydrochloride  $\text{C}_8\text{H}_{11}\text{NO}_2\cdot\text{HCl}$  at 99% by ACROS Organics ( $MW_{DOPA}=189.64$  g/mol).

As dopamine is quite expensive, calculation of the minimum quantity required for grafting was carried out, in order to use a quantity of dopamine lower than the protocol intended one.

It was supposed:

- Maximum quantity of grafted dopamine on surface to be  $1 \text{ molecule/nm}^2$ ;
- Nanoparticles to be spherical, with 10 nm diameter;
- NPs density to be equal to bulk maghemite density  $\delta=4.9\cdot 10^{-18} \text{ mg/nm}^3$ ;
- To graft 100 mg of NPs.

The procedure is reported in (2.3), where  $V_{TOT,NPs}$  is the volume of 100 mg of NPs,  $m_{NPs}$  the mass of NPs that is to be grafted,  $\delta_{magh}$  bulk maghemite density,  $A_{NP}$  the surface of a single NP and  $V_{NP}$  its volume,  $N_{NPs}$  the number of NPs contained in 100mg of them,  $V_{TOT,NPs}$  and  $A_{TOT,NPs}$  the volume and the surface respectively of 100mg of NPs,  $N_{DOPA}$  the number of dopamine molecule necessary and  $N_{Av}$  the Avogadro number.

$$\begin{aligned}
V_{TOT,NPs} &= \frac{m_{NPs}}{\delta_{magh}} \longrightarrow V_{TOT,NPs} = \frac{100}{4.9 \cdot 10^{-18}} = 2.04082 \cdot 10^{19} \text{ nm}^3 \\
A_{NP} &= 4\pi r^2 \longrightarrow A_{NP} = 4\pi(5)^2 = 314.159 \text{ nm}^2 \\
V_{NP} &= \frac{A_{NP} \cdot r^3}{3} \longrightarrow V_{NP} = \frac{314.159 \cdot 5}{3} = 523.599 \text{ nm}^3 \\
N_{NPs} &= \frac{V_{TOT,NPs}}{V_{NP}} = 3.898 \cdot 10^{16} \\
A_{TOT,NPs} &= A_{NP} \cdot N_{NP} = 1.2245 \cdot 10^{19} \text{ nm}^2 \\
N_{DOPA} &= A_{TOT,NPs} \cdot \delta_{surf,DOPA} \longrightarrow N_{DOPA} = 1.2245 \cdot 10^{19} \cdot 1 = 1.2245 \cdot 10^{19} \text{ molecules} \\
m_{DOPA} &= MW_{DOPA} \cdot \frac{N_{DOPA}}{N_{Av}} = 3.856 \text{ mg}
\end{aligned} \tag{2.3}$$

As it can be seen in (2.3), the effective amount of dopamine molecules required is about 4mg, if 1 molecule/nm<sup>2</sup> is supposed to be the expected grafting density.

Since grafting procedure must be carried out with an excess of dopamine, during this project 100 mg were added for grafting, instead of 5 g required by the previous protocol.

Concerning the other grafting steps, they had been reproduced following protocol parameters. As ultrasounds bath, it was used an Ultrasonic Cleaner by VWR.

When NPs-supernatant separation didn't succeed by magnet application, the suspension was separated by centrifugation (Beckman Coulter Avanti J-26 XP centrifuge) for 15 minutes at 22000 rpm and maximum deceleration.

The final NPs were dried under laboratory hood at room temperature overnight, since dopamine is sensible to temperature and it can degrade by heating.

This functionalization process was repeated several times, till about 2 g of dopamine-functionalised NPs (NPs DOPA) were obtained.

The novel grafting condition was then validated by IR spectroscopy and thermo-gravimetric analysis, performed to confirm the presence of dopamine on NPs surface.

### 2.2.3 The amino-silane

APTES is an organosilane bearing an amine function, with the structural formula reported in Table 2.3. It is reactive to water, so grafting is carried out by hydrolysis reaction. This consists on nucleophilic substitution of NPs surface hydroxyl groups onto APTES' silicon, determining a Si-O bond and an ethoxy group detachment, keeping intact the amine function.

The reaction outline is summarized in Figure 2.6.

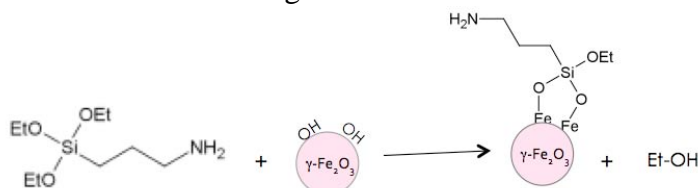


**Figure 2.6** Grafting reaction of APTES on maghemite NPs surface.

#### 2.2.3.1 APTES grafting protocol

APTES grafting looks back on procedure used by Caruntu<sup>31</sup> during his studies and it is the same followed by L. Ourry in the first part of the project.

40 mg of NPs are placed into a triple-neck round-bottom flask with 4 mL of methanol. The flask is put in ultrasonic bath for 2-3 minutes and, then, 100 mL of ethanol are added. The flask is put for other 2-3 minutes in ultrasonic bath.

400  $\mu$ L of APTES are now introduced and the solution is kept in stir for 1 hour with a mechanical stirrer.

Finally it is boiled for 2 hours under argon atmosphere and let at room temperature till it is cold.

Grafted NPs are separated from the supernatant by a magnet.

#### 2.2.3.2 Experimental working conditions

3-aminopropyl-triethoxysilane  $C_9H_{23}NO_3Si$  at 99% ( $MW_{APTES}=221.37g/mol$ ) by ACROS Organic was used.

Following protocol proportion, 120 mg of NPs were introduced in 12 mL of methanol inside a triple-neck flask. After 2-3 minutes of ultrasounds, 300 mL of ethanol were added. The flask was placed in ultrasound for other 2-3 minutes. 1200  $\mu$ L of APTES were put inside the flask.

The solution had been stirred for 1 hour at room temperature and then boiled for 2 hours under Ar atmosphere; the heater was set at 80°C and boiling point was observed at 78°C. Ethanol was regularly added during boiling, as it tends to evaporate.

After cooling down to room temperature, NPs were obtained with the assistance of a magnet.

#### *2.2.4 The amino-phosphonic acid*

3-aminopropylphosphonic acid (PHOSP) Lewis' formula is reported in Table 2.3. This molecule is known as a good ligand for  $Fe^{3+}$  ions.

Being not reactive to water like dopamine, it is grafted onto iron oxide NPs surface thanks to its chelating power. Complexation reaction is supposed to occur with  $\text{Fe}^{3+}$  ions on surface and the  $\sigma$ -donor ligand, as in Figure 2.7.

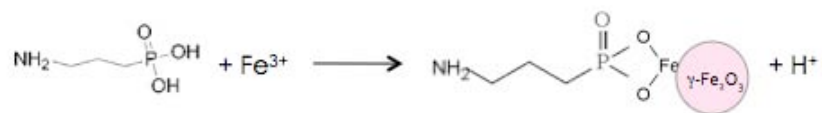


**Figure 2.7** Complexation reaction of  $\text{Fe}^{3+}$  ions by 3-aminopropylphosphonic acid.

#### 2.2.4.1 PHOSP grafting protocol

PHOSP grafting follows protocol used by N. Benjamaa during her work<sup>32</sup>.

50 mg of maghemite NPs are introduced in a 300 mL conical flask, together with 100 mL of Millipore water. NPs are dispersed under ultrasounds waves for 30 minutes.

Add 50 mg of PHOSP and homogenise the dispersion with ultrasound wave for 30 minutes, once again.

Let the flask rest upon a magnet for about 10 minutes and then throw away the supernatant separated from NPs, always keeping the magnet on the bottom of the conical flask.

At this moment grafted NPs must be washed 3 times using 100 mL of tetrahydrofuran (THF) each time and one last time with 100 mL of ethanol.

NPs are finally dried in an oven at 50°C.

#### 2.2.4.2 Experimental working conditions

3-aminopropylphosphonic acid  $\text{C}_3\text{H}_{10}\text{NO}_3\text{P}$  at 98% by Sigma Aldrich was used.

On the basis of the protocol, the quantity of reagents necessary to graft 150 mg of NPs was derived. Since it is the triple quantity of NPs than the one expected by the protocol, each reagent and solvent amount in paragraph §2.2.3.1 was multiplied by 3.

Every time THF or ethanol was added, the conical flask was placed 3 minutes in ultrasonic bath in order to homogenise the solution. During the washing with only THF or ethanol, the solvent stayed a little bit brownish.

## **2.3 Fluorophore grafting for drug mimicry**

### *2.3.1 Introduction*

Among the other purposes already exposed, NPs functionalization by amine groups is meant to attach drugs' molecules on particles surface.

In biological studies drugs behaviour is often simulated by organic fluorophore molecules, thanks to their similar chemical characteristics and to the possibility of directly follow them with optical absorption and fluorescence spectroscopy.

Fluorescein isothiocyanate (FITC) is quite commonly chosen for this kind of applications, owing to its biocompatibility.

From the chemical point of view, it is a derivative of fluorescein, in which an isothiocyanate reactive group  $-N=C=S$  replaces a hydrogen atom on the bottom ring of the structure as in Figure 2.8, used in wide-range applications of biological nature. This derivative is reactive towards nucleophiles, such as amine functions on biological molecules.

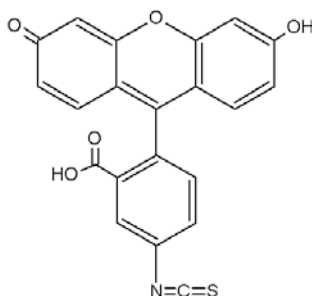


**Figure 2.8** Fluorescein isothiocyanate structural formula.

In this contest, the study is directed to FITC attachment on functionalized NPs surface by reaction with the amine groups carried by the ligands. A representation of such a system is showed in Figure 2.9.

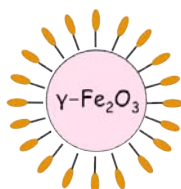


**Figure 2.9** Maghemite NP functionalized by amine groups (in grey) and grafted by FITC molecules (in orange) on such amine functions.

Fluorescent labelling was made on NPs grafted with each of the three different types of amine ligands, in order to collect data about their effectiveness in drug' trapping. Indeed, fluorescence spectroscopy analysis on such NPs (FITC NPs) were carried out and they permitted to compare the different spectra's peaks, which height corresponds to fluorescent emission intensity and can be associated to the amount of FITC molecules actually linked to NPs surface. Also simulating FITC NPs ageing had been possible, so comparing different ligands stability in water over time.

Like most fluorophores, FITC is prone to photobleaching but it was shown<sup>33</sup> to be superior in stability, ease of conjunction and degree of fluorescence in relation to other derivatives of fluorescein. It is sufficient to do fluorescence analysis not too long time after FITC grafting and to keep FITC grafted specimens at low temperature and no light exposed.

FITC has excitation fluorescence spectrum peak of approximately 495 nm and emission peak at 521 nm. Fluorescent spectroscopy will be based on these fundamentals data.

### 2.3.2 FITC labelling protocol

According to a validated protocol<sup>34</sup>, the solutions reported in Table 2.4 must be prepared in order to label NPs with FITC.

**Table 2.4** Solutions for FITC labelling on iron oxide NPs.

	Description	Concentration	Quantity to add
<b>Sol 1</b>	NPs in PBS buffer pH 7	1 mg/mL	121 $\mu$ L
<b>Sol 2</b>	FITC in NaHCO <sub>3</sub> 1M	10 mg/mL	27 $\mu$ L
<b>Sol 3</b>	NaCO <sub>3</sub> in distilled H <sub>2</sub> O	1M	10 $\mu$ L

Sol 1 and sol 2 are mixed up and added to sol 3, stirring overnight. The quantity of each solution added, depends on the amount of FITC that one wants to have upon NPs. The labelling process must be carried out at pH 9.25; this condition depends on relative quantity of each solution employed.

Assuming to have a final concentration equal to 20  $\mu$ g FITC/mg NPs, the quantity added for each solution is that reported in the last column of Table 2.4.

This protocol proves also that FITC labelling do not affect NPs properties, by mean of dynamic light scattering measurements.

### 2.3.3 Experimental procedure adopted for FITC labelling

First of all, NaHCO<sub>3</sub> and NaCO<sub>3</sub> 1M solutions were prepared dissolving the species listed in Table 2.5 in 15mL of distilled water.

**Table 2.5** Molar concentration, ponderal concentration of the solutions and amounts of NaHCO<sub>3</sub> and NaCO<sub>3</sub> dissolved in 15mL of water.

	Molar concentration	Mass concentration	Amount in 15mL H <sub>2</sub> O
<b>NaHCO<sub>3</sub></b>	1M	84.01 mg/mL	1260.15 mg
<b>NaCO<sub>3</sub></b>	1M	106.00 mg/mL	1590.00 mg

The test tubes for labelling solution preparation had been clothed with tinfoil, in order to protect their content from light.

Sol 1, sol 2 and sol 3 were then prepared on the basis of concentrations intended from Table 2.4, while each amounts to be added was multiplied by 30 in order to obtain more

solution and NPs for the characterization step (Table 2.6). This procedure was followed for each type of decorated NPs (DOPA, APTES and PHOSP).

**Table 2.6** Amount added for each solution in the present work.

	Amount added	V(sol1+sol2+sol3)
<b>Sol 1</b>	3.63 mL	4.737 mL
<b>Sol 2</b>	810 $\mu$ L	
<b>Sol 3</b>	297 $\mu$ L	

The labelling solutions were stirred over night in darkness with the swing mixer in Figure 2.10.

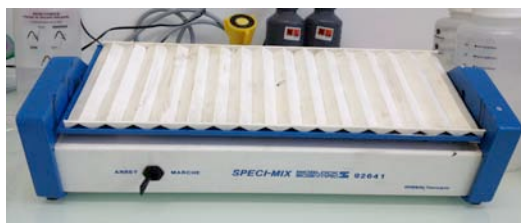


**Figure 2.10** Swinging shaker for FITC labeling.

After labelling, the test tubes were placed upon a magnet in order to separate FITC NPs from the supernatant. Indeed, the labelling solutions without NPs were then analysed by fluorescent spectroscopy to determine the amount of FITC that hadn't been adsorbed onto NPs surface and therefore left in solution. Those solutions were conserved in dark little bottles in order to prevent FITC degradation (Figure 2.11).



**Figure 2.11** Supernatant solution after FITC labelling in dark conserved in dark little bottles.

#### 2.3.4 FITC labelled NPs' ageing experimental process

FITC labelled NPs separated from the supernatant were re-dispersed in a volume of PBS equal to the initial labelling solution volume (4.737 mL) with ultrasound waves for 20 minutes. Temperature rising was controlled by regular introduction of ice inside the ultrasonic bath.

The solutions were placed again upon a magnet and the supernatant was collected for UV-Vis analysis when it was separated from NPs.

This ageing process was repeated two other times and the respective solutions were also preserved for analysis.

## **2.4 Biopolymer-based nanocomposite preparation**

### **2.4.1 Introduction**

The polymers, indicated in Table 1.1 as matrices, are all polysaccharides derived from natural sources, hence presenting advantages in terms of biocompatibility, biodegradability, low-toxicity and low cost. Indeed, polysaccharides are often used as nanocomposites matrix, thanks to their characteristics of relevance for biological and medical applications.

In addition to biocompatibility and the possibility to biofunctionalize their structure, an interesting property of such polymers is their sensitivity to external stimuli. Overall polysaccharides form gels that respond to physiological changes in temperature and pH or to mechanical stress. As instance, alginate<sup>35</sup> and chitosan<sup>36</sup> were used in preparation of magnetic composite hydrogels for magnetically triggered drug release; the application of a high-frequency magnetic field caused a local increase of the temperature of the embedded magnetic NPs that induced structural changes in the polymer matrix, thus leading to a controlled and enhanced release of the encapsulated drug.

#### **2.4.1.1 Preparative chemical strategies**

Two main types of strategies are generally employed for the preparation of polysaccharide based nanocomposites, that are the *in situ* and the *ex situ* synthesis.

The *in situ* strategies consist on the synthesis of inorganic nanofillers in the presence of the biopolymer and they allow a more intimate NPs dispersion within the polymer matrix. However the control over NPs size and shape in the presence of the polymers still remains a challenge; indeed, *in situ* synthesized NPs are generally size polydispersed and therefore they have limited application chances since most of inorganic fillers properties are size and shape dependent.

To overcome these limitation, the *ex situ* strategies is still quite prevalent consisting in the encapsulation of preformed inorganic NPs by the biopolymer. The use of this last type of strategies relies on the ability to produce NPs with required functionalities, as far as the size and shape dependent properties and also the presence of specific chemical groups at their surface (NPs functionalization). NPs are usually dispersed in water and then the



encapsulation can be performed by homogeneous mixing of NPs solution with an aqueous solution of the biopolymer, thanks to its hydrophilic nature.

## 2.4.2 The alginates as biopolymer matrix

### 2.4.2.1 Generalities

Alginates are hydrocolloids, water-soluble biopolymers extracted from brown seaweed (Figure 2.12), of polysaccharides family.

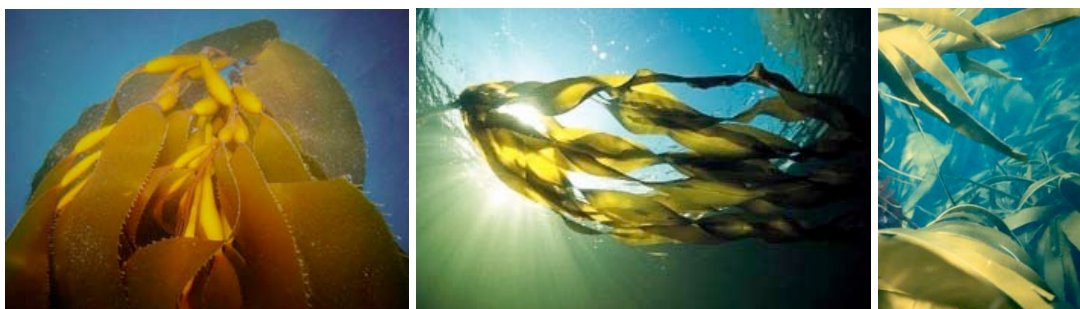


**Figure 2.12** Brown seaweeds. Images credits from left to right: Bio Architecture Lab and University of Karachi, Pakistan.

They were first researched in the late 19<sup>th</sup> century by the chemist E.C. Stanford, although it was about 50 years before they were produced commercially. Since that time, much about this versatile material have been discovered; not just new knowledge of its multiple properties, such as gelling, film-forming, thickening and stabilizing characteristics, but also how to adjust harvesting and processing methods to enhance those properties have been investigated.

Alginate occurs naturally mainly in cell walls of brown algae in the form of calcium, magnesium and sodium salts; then, specific processes were developed to extract alginate while completely removing all other biological and inorganic impurities.

### 2.4.2.2 The structure

From the chemical point of view, alginates are made up of blocks of mannuronic acid and guluronic acid, the composition of which depends on the species used for extraction and the part of alga from which extraction is executed.

When extracting alginates from harvested material, the uronic acids are converted into the salt forms mannurate (M) and guluronate (G) through a neutralization step. Alginate definitely is a block copolymer composed of longer homopolymeric regions of M or G, potentially separated by regions alternating structure (MG). While G-blocks provide gel-forming capacity, MM and MG units provide flexibility to the chains, with flexibility increasing in the following order: GG<MM<MG. The proportion, distribution and length

of these blocks determine the chemical and physical properties of the alginate molecules. In Figure 2.13 the monomers and an example of copolymer are reported.

Alginate polymers are negatively charged and they have a negative charge for each monomer upon the carboxylate function on C<sub>6</sub>: thus they are considered good polyelectrolytes.

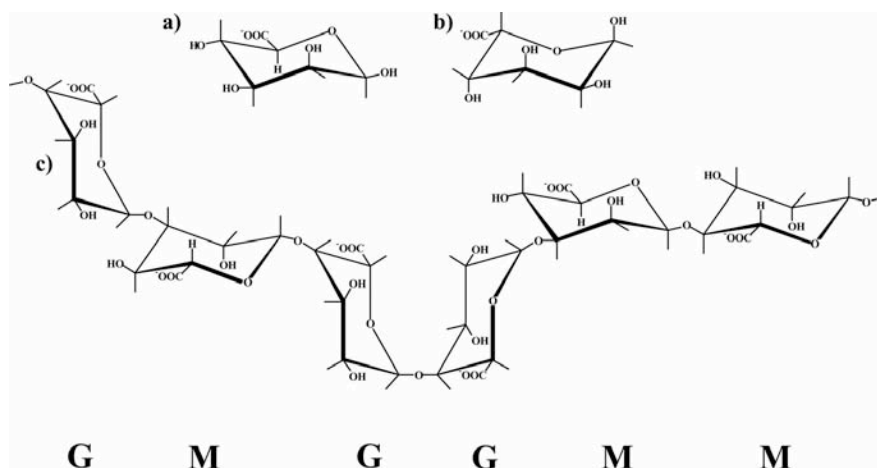


**Figure 2.13** a)  $\beta$ -D-Mannuronic acid (M); b)  $\alpha$ -L-guluronic acid (G); c) block copolymer structure.

#### 2.4.2.3 Viscosity and gel formation

The viscosity of an alginate solution depends on the alginate concentration and length of the alginate molecules, or the number of monomer units in the chains, with longer chains resulting in higher viscosities at similar concentrations.

Aqueous solutions of alginate have shear-thinning characteristics, meaning that viscosity decreases as the shear rate or stirring speed increases. This property is known as pseudoplasticity; temperature will influence viscosity as well, with increasing temperature resulting in decreased viscosity.

Moreover, alginate structure is related to the ability to form a gel, according to the proportion and length of G-blocks in its molecular structure.

In particular, regions of guluronate monomers that are G-blocks, in one alginate molecule can be linked to a similar region in another alginate molecule by means of multivalent cations, like calcium ions  $\text{Ca}^{2+}$ . The divalent calcium cations fits into the guluronate block structure like eggs in an *egg box*, binding the alginate chains together by forming junction zones, resulting in gelation of the solution. An example of formation of the *egg box* structure is that in Figure 2.14.

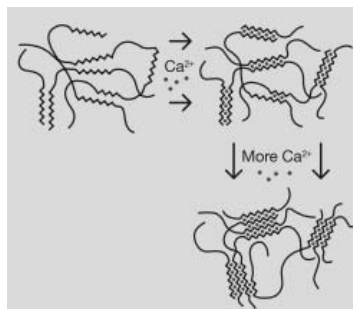


**Figure 2.14** Egg box structure in gel formation by alginate chains<sup>37</sup>.

Once formed, an alginate gel may be considered part solid and part solution; water and other molecules are physically trapped within the alginate matrix by capillary forces, yet remain free to migrate by diffusion, depending on size. This property makes alginate gels ideals for multiple applications, including encapsulation.

There are three main components in a typical alginate gelling system: alginate, calcium ions and sequestrant. Alginate type and counter-ion, calcium source and the sequestering agent control the gelling system structure and the rate at which the gel forms.

### ***2.4.3 Experimental procedure for alginate-based nanocomposite preparation***

#### **2.4.3.1 Alginate solution preparation**

During this study sodium alginate by Sigma Aldrich in the form of brown powder was used.

Alginate solutions and nanocomposites with DOPA NPs were prepared in the MSC laboratory of Paris Diderot University by D. Braccagni during his master research activity. First, a mother solution of sodium alginate was prepared adding 1.5 g of powdery alginate to 30 mL of distilled water and stirring the solution for 24 hours at 410 rpm.

Then, an alginate solution with 18 g/L concentration was prepared, using the alginate mother solution.

1.8 mL of 50 g/L alginate solution was diluted to volume with 0.7 mL of distilled water and then mechanically stirred for 20 minutes.

#### **2.4.3.2 Decorated NPs addition to alginate solution**

Another mother solution with 1% in volume of DOPA NPs was prepared weighing 250 mg of DOPA NPs and diluting to volume with 5 mL of distilled water; NPs were dispersed by 15 minutes of ultrasounds bath.

Finally 2.5 mL of this NPs solution were added to 18 g/L solution of alginate, previously prepared, and stirred for 5 minutes with a vortex.

The solution obtained was brown after the introduction of iron oxide NPs.



# Chapter 3

## Characterisation Methods

In the following chapter various methods adopted for NPs and nanocomposites characterisation will be presented, along with experimental parameters and procedures observed during this study. The chapter is divided in different paragraphs treating each type of material synthesized during the experimental section.

### 3.1 Bare and decorated nanoparticles

#### 3.1.1 *Infra-Red spectroscopy*

##### 3.1.1.1 Methods

Infrared (IR) spectroscopy is the absorption measurement of different IR frequencies by a sample positioned in front of an IR beam. The main goal of IR spectroscopy analysis is to determine the chemical functional groups in the sample, since different functional groups absorb characteristic frequencies of IR radiation. Using various sampling accessories, IR spectrometers can accept a wide range of sample types such as gases, liquids, solids and powders too.

IR absorption information is generally presented in the form of a spectrum with wavelength or wave number as the x-axis and absorption intensity or percent transmittance as the y-axis. Transmittance  $T$  is the ratio of radiant power transmitted by the sample ( $I$ ) to the radiant power incident on the sample ( $I_0$ ), while absorbance  $A$  is the logarithm to base 10 of the reciprocal of  $T$ ; the relation between  $A$  and  $T$  is defined in (3.1).

$$A = -\log_{10} T = -\log_{10} \frac{I}{I_0} \quad (3.1)$$

The transmittance spectra provide better contrast between intensities of strong and weak bands because transmittance ranges from 0 to 100% whereas absorbance ranges from infinity to 0.

The most frequently used IR region is the one between 4000 and 400  $\text{cm}^{-1}$  that is 2.5 to 25  $\mu\text{m}$  of wavelength. When infrared radiation is absorbed, the associated energy is converted into molecular vibration modes, above all stretching and bending (Figure 3.1). The absorption involves discrete, quantized energy levels, even if other rotational motions

usually accompany the individual vibration motion; these combination lead to absorption bands, not discrete lines, commonly observed in the mid region.

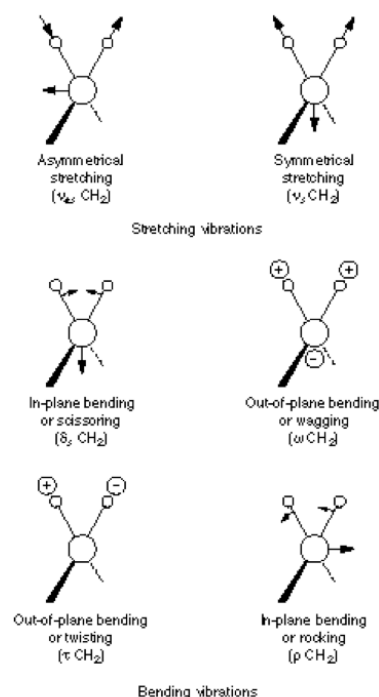


**Figure 3.1** Stretching and bending vibrational modes.

A Fourier transform spectrometer was used in the present study due to his superior speed and sensitivity. Instead of viewing each component frequency sequentially, in Fourier transform infrared (FTIR) spectroscopy all frequencies are examined simultaneously. Moreover, an attenuated total reflectance (ATR) accessory was introduced, being especially useful for obtaining IR spectra of difficult sample that cannot be readily examined by normal transmission methods, such us nano-powders. Indeed, ATR requires little sample preparation.

ATR occurs when a beam of radiation enters from a medium with a higher refractive index to a medium with a lower refractive index; the fraction of the incident beam reflected increases when the angle of incidence increases. All incident radiation is completely reflected at the interface when the angle of incidence is greater than a critical angle related to the refractive index.

The sample is normally placed in close contact with a more-dense, high-refractive-index crystal, in this case germanium. The IR beam is directed onto the bevelled edge of the ATR crystal and internally reflected through the crystal with a single or multiple reflections. The beam penetrates a very short distance beyond the interface and into the less-dense medium before the complete reflection occurs; this penetration is called the evanescence wave and

its intensity is attenuated by sample in regions of the IR spectrum where the sample absorbs.

The resulting ATR-IR spectrum resembles the conventional IR spectrum, but with some differences: the absorption band positions are identical in the two spectra, but the relative intensities of corresponding bands are different.

Figure 3.2 illustrates the basic ATR principles.

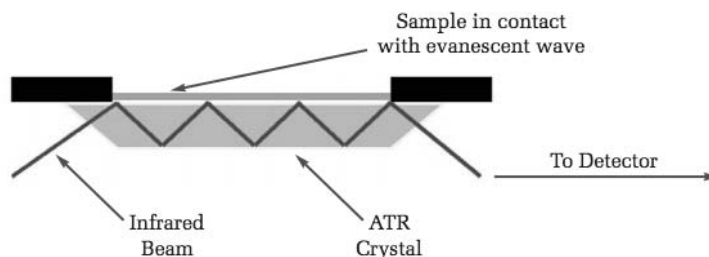


**Figure 3.2** Schematic representation of multiple internal reflection effect in ATR.

#### 3.1.1.2 Experimental procedure

The spectrometer Nicolet 8700 with the Varig ATR accessory was used for the analysis, while data were elaborated by the software OMNIC in a range of wavenumber between  $4000\text{cm}^{-1}$  and  $550\text{cm}^{-1}$ .

The background spectrum was recorded before each sample spectrum acquisition, in order to subtract atmosphere's elements from sample composition.

A NPs' point of spatula was enough to conduct the analysis. Those were placed upon the germanium crystal of the sample holder, covered with a microscope glass slide that doesn't absorb in IR range and then pressed with a powder tip.

### **3.1.2 X-Ray diffraction (XRD)**

#### 3.1.2.1 Methods

X-ray diffraction (XRD) is a rapid analytical technique mainly used for phase identification of a crystalline material and collecting information on unit cell dimensions. It must be pointed out that if the analysed sample is constituted of nanometer-sized NPs, the unit cell dimension can be considered equal to NPs diameter.

Generally, atoms are disposed inside a crystal in a regular tri-dimensional periodic array, while X-rays have wavelength  $\lambda$  typically of the same order of magnitude as the spacing  $d$  between planes in the crystal. Thus, X-ray diffraction occurs when a monochromatic electromagnetic ray of such a value of  $\lambda$  impinges on a regular array of atoms.

Atoms scatter x-rays wave primarily through the atoms' electrons; in particular, an x-ray striking an electron produces secondary spherical waves from the electron itself, establishing a phenomenon known as *elastic scattering*, while electrons are the *scatterer*.

The waves created from the electrons generally cancel themselves each other because of their destructive interference, but in few specific directions they may also interfere constructively; such directions are determined by Bragg's law (3.2), where  $n$  is an integer number,  $\lambda$  is the beam wavelength,  $d$  is the space between crystalline planes and  $\theta$  is the angle formed between the incoming beam and the plane's direction.

$$n\lambda = 2d \sin \theta \quad (3.2)$$

To better understand Bragg's law, in Figure 3.3 a schematic representation of X-ray diffraction phenomenon is reported.

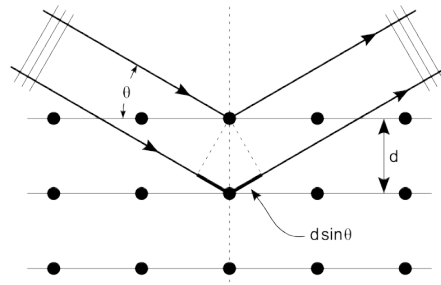


**Figure 3.3** X-ray diffraction scheme: constructive interference.

The incoming beam is scattered by atoms placed in different crystalline planes and the spherical waves produced by wave-atoms interaction will be in sync only in direction where their path-length difference ( $2d \sin \theta$ ) equals an integer multiple of  $\lambda$ . In this case the interference is constructive and it produces a spot at  $2\theta$  in the diffractogram.

Since only the families of planes (hkl) parallel to detector's plane can be analysed, the detecting system, composed by the X-ray beam and the detector, rotates around the sample in order to collect information about all the present planes.

The intensity of the diffracted rays is measured and reported in a diagram in relation to the angle  $2\theta$ ; such a diagram is called diffractogram.

The area included under the peak is proportional to the diffracted intensity and gives information about the crystalline phase of the sample, which can be determined consulting a database created by the Joint Committee for Powder Diffraction Standard.

Moreover XRD has a good potential for the analysis of nano-structures' size range, because the width and shape of reflections yield information about the substructure of the materials. There are several approaches to analyse X-ray diffraction profile in order to find information about structure's size, between which Scherrer and Williamson-Hall methods are the most widely applied. Both these methods consider width profile but not its shape.



Williamson-Hall method, unlike the Scherrer one, allows eliminating structural aberration rate from the calculation. Anyway, in this report the Scherrer method is employed since the percentage amount of aberration in the structure can be considered equal to zero.

Cristalline size resulting from Scherrer equation (3.3) can be considered equal to particles mean size  $D_{NPs}$  only when they are on the nanometer size-range.

$$D_{NPs} = \frac{k\lambda}{\beta \cos \theta} \quad (3.3)$$

In (3.3)  $k$  is a shape factor close to unit, usually about 0.9,  $\lambda$  the wavelength of the incident X-ray beam,  $\beta$  is the line broadening at half the maximum intensity in radians, after subtracting the instrumental line broadening,  $\theta$  is the Bragg angle.

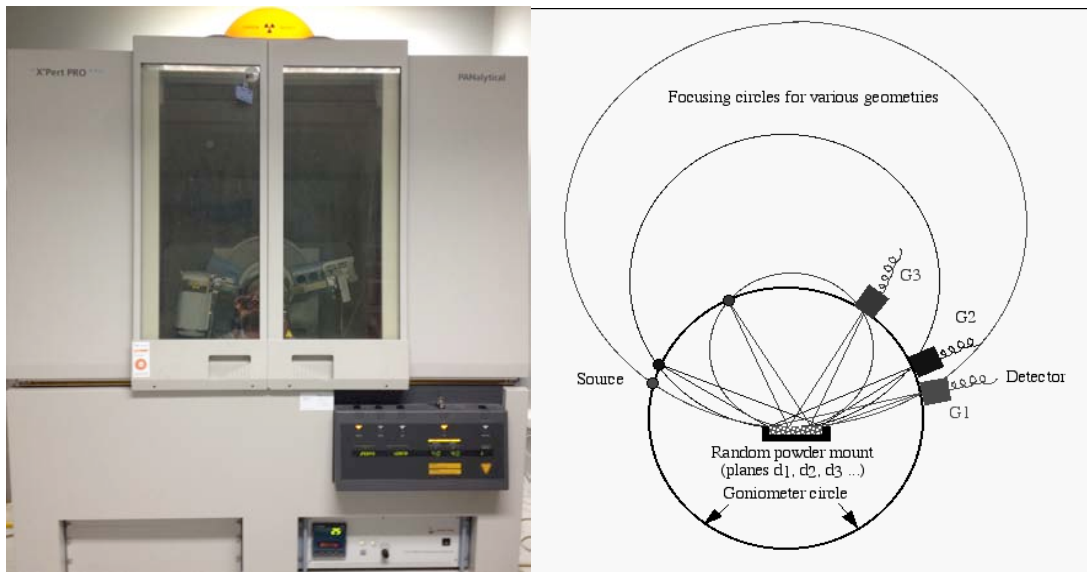


**Figure 3.4** PANalytical X'Pert PRO XRD diffractometer (left) and Bragg-Brentano geometry (right)

### 3.1.1.2 Experimental procedure

XRD measurements were carried out by the PANalytical X'Pert PRO diffractometer in Figure 3.4 (left), with a multichannel detector X'celerator and a cobalt anticathode ( $\lambda_{CoK\alpha1}=1.7889\text{\AA}$ ).

The sample is placed in the centre of a vertical goniometer of Bragg-Brentano geometry (Figure 3.4 right), while the X-ray tube and the detector turn in an angular range between  $10^\circ$  and  $110^\circ$  with a step of  $0.02^\circ$ .

Radiation is emitted from a tungsten filament heated by an electricity of 40 kV and 40 mA. The samples are prepared in such a way that their surface is as planner as possible; for this reason the powder is previously crushed in a mortar allowing also a reorganization of the crystalline planes.

### 3.1.3 Transmission Electron Microscopy (TEM)

#### 3.1.3.1 Methods

TEM is a vital characterization tool for directly imaging nanometer-sized materials to obtain quantitative measures of particles or grain size, size distribution and morphology. The transmission electron microscope (TEM) operates on many of the same optical principles as the light microscope, but it has the added advantage of greater resolution.

In fact, this type of electron microscopy allows imaging the transmission of a focused electrons beam through a sample, forming an image analogous to a light microscope image. Because electrons are used as “light source” and their wavelength is much lower than the light one, TEM imaging has a thousand times higher resolution than light-based imaging techniques.

With light microscopes it is possible to observe objects to a limited field at the light wavelength, while TEM allows investigation of objects to the order of a few of Angstrom. A schematic representation of TEM’s architecture is in Figure 3.5. An electron source at the top of the structure emits the electrons that travel through vacuum in the column of the microscope. Electromagnetic lenses are used to focus electrons in a very thin beam, which is then directed through the specimen.

Amplitude and phase variations in the transmitted beam provide imaging contrast, in relation to the amount of material that the electron beam pass through and the sample material: heavier atoms scatter more electrons and therefore have a smaller electron mean free path than lighter atoms. Depending on the density of the specimen material some electrons may be scattered and disappear from the beam.

At the bottom of the microscope the unscattered electrons hit a fluorescent screen, which gave rise to a shadow image of the specimen with its different parts displayed in varied darkness according to their density.

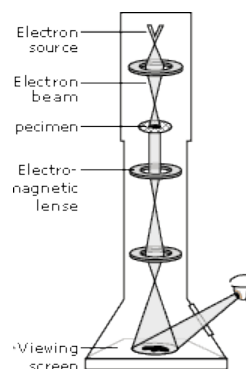


**Figure 3.5** Schematic representation of TEM architecture.

Since electrons are very small and easily deflected by hydrocarbons or gas molecules, it is necessary to induce a vacuum environment; a series of pumps are used to accomplish an adequate vacuum for this purpose.

Successful imaging of NPs using TEM depends on the contrast of the sample relative to the background. Samples must be properly prepared for imaging by drying NPs on a copper grid that is coated with a thin layer of carbon. Materials, such as magnetic NPs, have electron densities higher than amorphous carbon and therefore they can be easily imaged.

A small drop of NPs suspension is placed onto the grid and allowed to evaporate, typically under vacuum. The concentration of NPs in suspension is a very important feature in sample preparation, since high concentration may lead to particles agglomeration while low concentration may occurs in not enough particles to analyse.

The images provided by TEM are later processed with software, used to measure particle dimensions, calculate their average size and their size distribution. In the present work the software SAISAM was employed at this aim.



*Figure 3.6 JEM 100CX-II by Jeol, transmission electron microscope.*

#### 3.1.3.2 Experimental procedure

The transmission electron microscope used was a Jeol JEM 100CX-II (Figure 3.6). The electron source is a tungsten filament with a tension of 100kV.

### **3.1.4 Thermo-Gravimetric Analysis (TGA)**

#### 3.1.4.1 Methods

Thermogravimetry (TG) or TGA is the branch of thermal analysis, which examines the mass change of a sample as a function of temperature in the scanning mode or as a function of time in the isothermal mode. Not all thermal events bring changes in the mass of the sample, for example melting, crystallization or glass transition, but there are some very important exceptions to this, like desorption, absorption, sublimation, vaporization, oxidation, reduction and decomposition.

TGA is used to characterize the decomposition and thermal stability of materials under a variety of conditions and to examine the kinetics of the physicochemical processes occurring in the sample.

The mass change characteristics of a material are strongly dependent on the experimental conditions employed. Factors such as sample mass, volume and physical form, the shape and nature of the sample holder, the nature and pressure of the atmosphere in the sample chamber, and the scanning rate have significant influences on the characteristics of the recorded TG curve. TGA makes a continuous weighing of a small sample in a controlled atmosphere (e.g., air or nitrogen) as the temperature is increased at a programmed linear rate.

The components of such an instrument are the microbalance, the furnace, the programmer controller, and a computer or data acquisition system; the sample pan is supported by a precision balance, placed in a furnace that heat or cool the sample during the analysis while the mass of the sample is monitored.

The measurement is normally carried out in air or in an inert atmosphere, such as Helium or Argon, and the weight is recorded as a function of increasing temperature. Sometimes, the measurement is performed in a lean oxygen atmosphere (1 to 5% O<sub>2</sub> in N<sub>2</sub> or He) to slow down oxidation. In addition to weight changes, some instruments also record the temperature difference between the specimen and one or more reference pans (differential thermal analysis, or DTA) or the heat flow into the specimen pan compared to that of the reference pan (differential scanning calorimetry, or DSC). The latter can be used to monitor the energy released or absorbed via chemical reactions during the heating process.

Thermogravimetric curves are characteristic for a given compound because of the unique sequence of the physiochemical reaction that occurs over specific temperature ranges and heating rates and are function of the molecular structure. These curves are normally plotted with the mass change  $\Delta m$  expressed as a percentage on the y-axis and temperature  $T$  or time  $t$  on the x-axis. A mass loss is often linked to physisorbed species' desorption (endothermic transition), decomposition, evaporation or reduction, while a mass gain to oxidation, absorption or to allotropic transformations (exothermic transitions). The mass loss occurs at different temperatures for each component: this concept is the basis of compositional analysis.



*Figure 3.7 SETARAM TGA-DTA 92 thermo-analysis system.*

#### 3.1.4.2 Experimental procedure

The instrument used for thermo-gravimetric analysis was a SETARAM TGA-DTA 92 (Figure 3.7) with an electromagnetic compensated microbalance. The temperature was raised from room values to 1000°C, with heating rate of 5°C/min. The pan that held samples was in platinum or alumina, while measurements were executed in air atmosphere.

### *3.1.5 Zeta potential measurements*

#### 3.1.5.1 Methods

The measurement of Zeta Potential is critical in understanding the electrical charge characteristics of sample particles. The electrical charge properties control the interactions between particles and therefore determine the overall behaviour of a sample suspension. Determining the stability of a sample, for example to minimize aggregation for drug delivery and pharmaceutical applications (high zeta potential required), it is of great importance in nanosciences field.

All materials will spontaneously acquire a surface electrical charge when brought into contact with a polar medium like water. The distribution of electrical charges at the interface results to be different from that in the bulk liquid phase; an electric double-layer is developed such that the particle surface charge is neutralized by an adjacent layer of ions of opposite charge to that of the surface. These ions are called counter-ions.

In this way, a particle in a liquid suspension is characterised by a surface charge that attracts a thin layer of counter-ions in the region surrounding the particle itself. The extent of the solvated layer around the particle is influenced by the solution characteristics, such as composition, temperature and pressure.

A representation of the solvated particles in suspension is reported in Figure 3.8, where it can be noticed the *Stern layer* (or fixed layer) that is a rigid layer of ions tightly bound to particle; the boundary of the Stern layer is called *Stern plane*. Outside this region there is the *diffuse layer*; inside the diffuse layer it can be defined the *slipping plane* that separates the ion moving with the particle when it travels, from which that do not move with it.

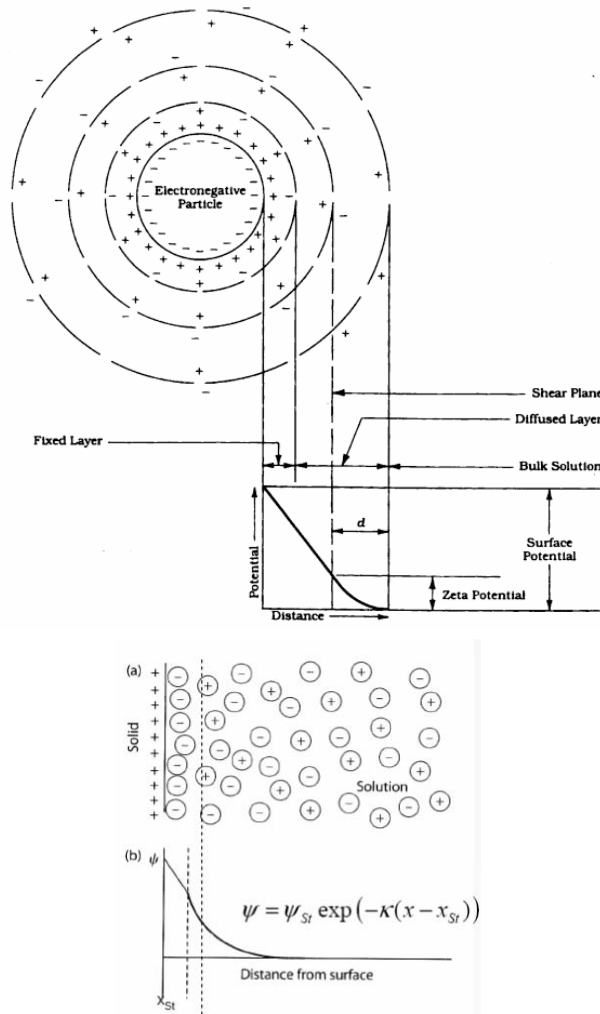


**Figure 3.8** Solvated particle in a polar medium: formation of various layers with different charge density is evidenced (left). Zeta potential values in relation to distance from particle's surface (right).

The charge distribution created around the particle gives rise to an electric potential at the surface that decreases moving through the bulk solution away from the surface.

The potential at the shear plane is known as *zeta potential* ( $\zeta$ ) and the pH, at which the zeta potential is zero, i.e. where there is no net charge at the slipping plane, is called *isoelectric point IEP*. The zeta potential value changes with pH of the suspension in which particles are dispersed and, on the other hand, IEP occurs at specific values for each material. Therefore, controlling the particle surface charge is possible so determining its zeta

potential value and guaranteeing the electrostatic stability of a NPs suspension; flocculation and precipitation will occur if the electrical repulsion between the particles doesn't exceed the attractive Van der Waals forces between them. NPs with  $\zeta$  more positive than +30mV or more negative than -30mV are considered stable.

Zeta potential values can be determined by measurement of electro-kinetic phenomena. Indeed, the NPs electrophoretic mobility, i.e. the speed that they achieve in an electric field, is linearly related to their  $\zeta$  potential.

### 3.1.5.2 Experimental procedure

In this study Malvern Zetasizer Nano ZS was used for  $\zeta$  potential the measurements (Figure 3.9.a), which bases its function on laser doppler micro-electrophoresis. An electric field is applied to a dispersion of particle contained in a folded capillary cell with gold electrodes on both sides, properly for zeta potential measurements such as the one in Figure 3.9.b and 3.9.c; after electric field application, the particles in suspension start moving with a velocity related to their zeta potential. This velocity is measured using a patented laser interferometric technique, called M3-Phase Analysis Light Scattering, that enables the software to calculate the electrophoretic mobility and from this the zeta potential and its distribution.

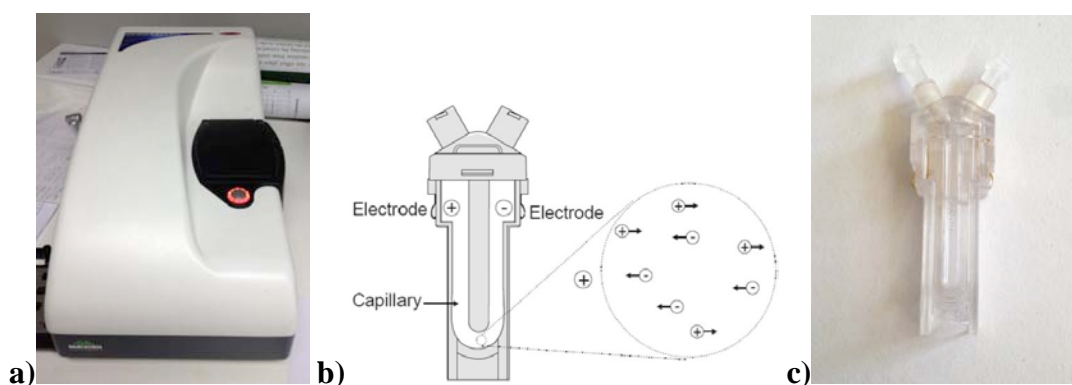


**Figure 3.9** *a) Malvern Zetasizer Nano ZS instrument for  $\zeta$ -potential measurements.  
b) Charge displacement inside the capillary folded cell under electric field application.  
c) Capillary folded cell with gold electrodes by Malvern Instruments for  $\zeta$  potential measurements.*

Solutions with pH ranging from 1 to 13 were prepared mixing distilled water and HCl or  $\text{NH}_3$  for acid or basic pH respectively. Solution preparation was conducted by gradual addition of HCl or  $\text{NH}_3$  drops with a micropipette, while pH was measured in the same time with a JENCO Electronics Microcomputer pH-VISION 6071 pH-meter.

When the desired pH was reached, solution was preserved in little glass bottle and later used to suspend the differently decorated NPs (Figure 3.10).

Bare NPs, DOPA NPs, APTES NPs and PHOSP NPs were dispersed in each solution from pH 1 to pH 13 with ultrasound waves for 3 minutes and their  $\zeta$  potential measured in previously described manner, with the main goal to take information about how NPs IEP change in relation to NPs' surface decoration. Each measurement was repeated three times and then the average of these was considered in the diagram drawing.

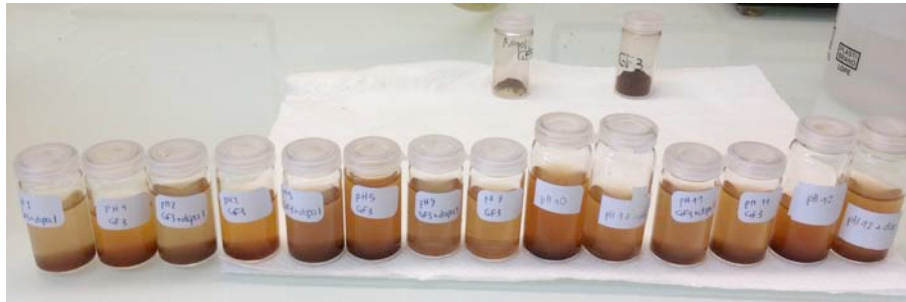


**Figure 3.10** Some bare and DOPA NPs suspensions at different pH used for  $\zeta$  potential measurements.

### 3.1.6 Superconducting Quantum Interference Device (SQUID) for magnetic measurements

#### 3.1.6.1 Methods

The material's response after a magnetic field application gives chemical and structural information.

Each paramagnetic cation has a magnetic moment  $\vec{\mu}$  that is oriented by the application of an external magnetic field  $\vec{H}$  in its same direction. Thus the material gets a magnetization  $\vec{M}$  equivalent to the sum of the individual magnetic cations' moments. By this, is possible to study  $\vec{M}$  evolution in relation to temperature when the magnetic field is kept constant or in relation to magnetic field when temperature is fixed.

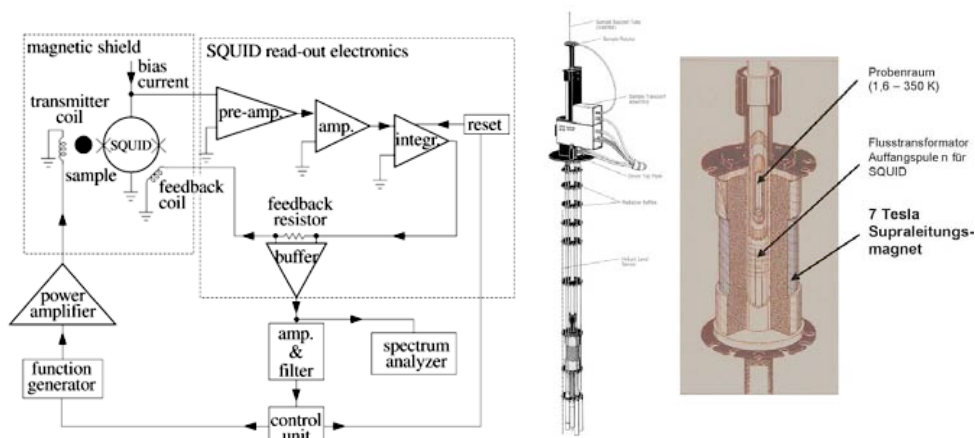


**Figure 3.11** SQUID magnetometer schematic representation.



The sample is placed inside a holder in the middle of three superconductive coils group, vertically disposed. The extreme coils have  $N$  turns coiled in the same way, while the middle coil has  $2N$  turns and it is coiled in the opposite way. This configuration permits to avoid the influence of currents induced by external magnetic field variations.

The sample is displaced along the coils' axis, generating a magnetic flux variation. These flux variations are transmitted to SQUID by an intermediate coil. The SQUID is a niobium-titanium superconductor ring, interrupted by a Josephson junction cooled under his transition temperature, which may induce an electric current  $I$  in order to compensate the flux variations. This electric current can be detected thanks to a network with resonance frequency of some MHz coupled to SQUID.

### 3.1.6.2 Experimental procedure

Magnetic measurements were executed with a SQUID instrument Quantum Design MPMS-5S. These measurements consisted in magnetization observation at 310 K under a magnetic field oscillating between +50 Oe and -50 Oe. NPs were compressed in a plastic diamagnetic capsule in order to minimize their movement during the measurements.

## **3.2 FITC labelled nanoparticles**

### *3.2.1 Ultraviolet-visible (UV-Vis) spectroscopy*

#### 3.2.1.1 Methods

Ultraviolet and visible lights are energetic enough to promote outer electrons in molecules bonds to higher energy levels. Valence electrons can generally be found in one of three types of electron orbital:

- Single or  $\sigma$  bonding orbitals;
- Double or triple bonds, that are  $\pi$  bonding orbitals;
- Non-bonding orbitals that are lonely pair electrons.

$\sigma$  Bonding orbitals tend to be lower in energy than  $\pi$  bonding orbitals, which in turn are lower in energy than non-bonding orbitals. When electromagnetic radiation of the correct frequency is absorbed, a transition occurs from one of these orbitals to an empty one, usually an antibonding orbital  $\sigma^*$  or  $\pi^*$  (Figure 3.12).

The exact energy difference between the orbitals depends on the atoms present and the nature of the bonding.

UV-Vis absorption spectroscopy is the measurement of the attenuation of a light beam after it passes through a sample or after reflection from a sample surface. Absorption measurements can be at a single wavelength or over an extended spectral range.

Organic fluorophore molecules typically absorb ultraviolet/visible radiation because of the presence of a particular functional group. FITC, for example, absorbs light with wavelength of about 495 nm leading to a fluorescence emission maximum around 521 nm; moreover it has a high quantum yield and approximately half of the absorbed photons are emitted as fluorescent light.

The UV-Vis spectra have broad features that are of limited use for sample identification but very useful for quantitative measurements.

In conventional spectrometers, electromagnetic radiation is passed through the sample in a small cell. Radiation across the whole of the UV-Vis range is scanned over a period of about 30 seconds and radiation of the same frequency and intensity is simultaneously passed through a reference cell containing only the solvent. Photocells then detect the radiation transmitted and the spectrometer records the absorption by comparing the difference between the intensity of the radiation passing through the sample and the reference cells.

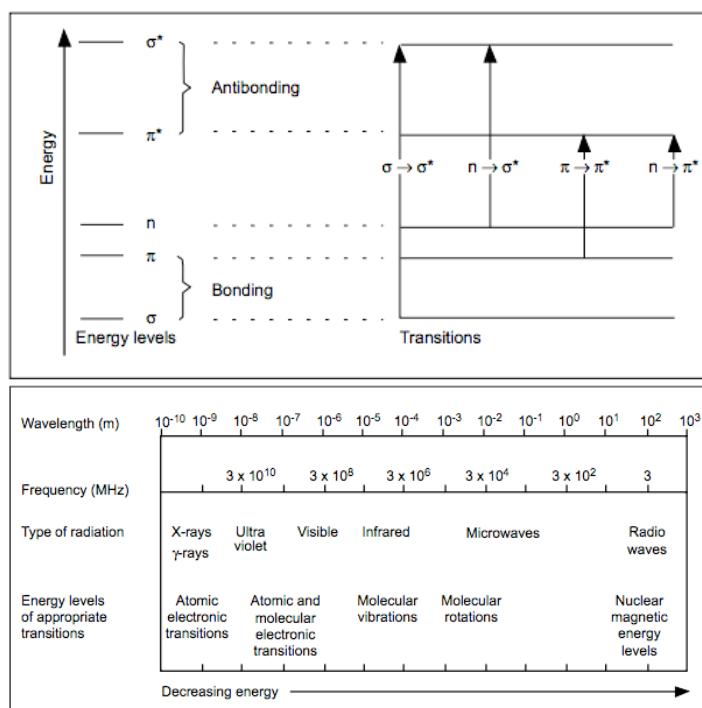


**Figure 3.12** Electron transitions in UV-Vis spectroscopy (upper) and electromagnetic spectrum regions (bottom).

In the latest spectrometers, radiation across the whole range is monitored simultaneously and the reference is automatically recorded.

A hydrogen or deuterium lamp covers the UV range of incident radiation and a tungsten filament covers the visible range. A diffraction grating followed by a narrow slit according

to its wavelength separates the radiation; the slit ensures the radiation to be monochromatic.

The cells that contain samples must be of pure silica for UV absorption analysis, because soda glass absorbs below 365 nm and pyrex glass below 320 nm.

The detection of radiation passing through the sample or reference cell can be achieved by either a photomultiplier or a photodiode that converts photons of radiation into tiny electrical currents.

Comparing the currents generated by the sample and the reference beams, the spectrum is produced. Modern instruments are self-calibrating, though the accuracy of the calibration can be checked if necessary. Wavelength checks are made by passing the sample beam through glass samples that have precise absorption peaks, and the absorption is calibrated by passing the sample beam through either a series of filters, each with a specific and known absorption, or a series of standard solutions. Figure 3.13 schematically represents how a UV-Vis spectrometer works.

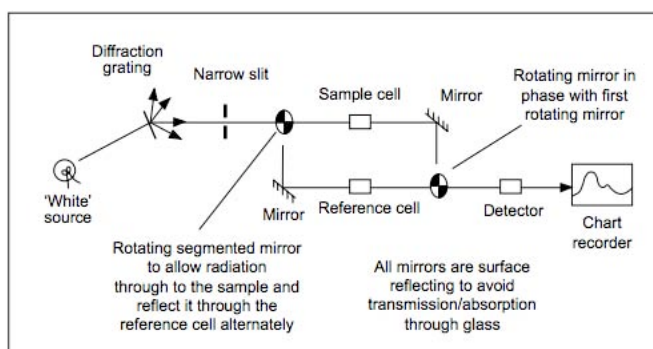


**Figure 3.13** Schematic diagram of UV-Vis spectrometer architecture.

Typically only small numbers of absorbing molecules are required for the analysis, so it is convenient to have samples in solution, with solvent that doesn't absorb in the UV-Vis range. The relation between the absorbance  $A$  of a specimen and the concentration  $C$  of analyte in solution defines *Lambert-Beer law* (3.4).

$$A = \varepsilon \cdot l \cdot C \quad (3.4)$$

$\varepsilon$  Is the molar extinction coefficient typical for each absorbing material and  $l$  is the path length of the absorbing solution in cm, generally equal to cell's width. When  $\varepsilon$  and the wavelength  $\lambda_{max}$  at which maximum absorption occurs are known, it is possible to identify a specific substance, although identification is not the most common use of this technique. Conversely, if  $\varepsilon$  and  $\lambda_{max}$  are known, the concentration of the solution can be calculated: this is the more common application.

### 3.2.1.2 Experimental procedure



**Figure 3.14** Perkin Elmer Lambda 1050 UV/VIS/NIR spectrometer.

A Perkin Elmer Lambda 1050 UV/VIS/NIR spectrometer (Figure 3.14) was used for UV-Vis absorption analysis, equipped of InGaAs and PbS 3-detector module for testing across the entire UV/Vis/NIR range. The cooled InGaAs allows to extend the spectral range up to 2500nm and because of its high sensitivity it is possible to set resolution down to 0.2nm.

Absorbance spectra were recorded for wavelength from 200nm to 800nm; the incident light beam was chosen with wavelength similar to  $\lambda_{max}$  that is 495nm, in order to reach the maximum of sample excitation.

A plastic cell 0.2mm wide was used to hold 3mL of solution, since plastic doesn't absorb energy in the range of considered wavelength.

The FITC molar extinction coefficient  $\epsilon_{FITC}$  is high and equal 77000 L/(mol cm), so it gives rise to very high absorbance values, according to Lambert-Beer law (3.4), and thus rough spectra with undefined peaks.

In order to obtain appropriate spectra with defined peaks, the absorbance entity was controlled on the basis of relation (3.4):

- Path length  $l$  was reduced to 0.2mm using a thin cell as sample holder;
- FITC concentration of the solutions was reduced before analysis, diluting a volume of the obtained labelling solutions with the same volume of distilled water.

Thus, before analysing labelling solutions of DOPA NPs, APTES NPs and PHOSP NPs, they were diluted with the proper dilution and the base line was recorded for each measurement by the UV-Vis spectrometer when no sample was introduced.

Washing solutions from the ageing process, instead, were directly analysed as-collected, without further dilution. Their spectra permitted to study absorbed FITC stability upon NPs surface.

A calibration line was defined measuring absorbance of the FITC solution before labelling at three different dilutions; the concentration of FITC in each solution is known and calculated considering the FITC and solvents mixed together before labelling.

Therefore, a relation between absorbance and FITC concentration in solution was found out and then used to determine the concentration of FITC in each solution after NPs

labelling, from the absorbance values obtained in each spectrum. In other words, this technique permitted to understand which one ligand on NPs surface permits to reach the best result in quantity and stability of FITC trapping.

### 3.3 Alginate-based nanocomposites

#### 3.3.1 Rheological basic concepts

Rheology is the study of flow and deformation of matter under applied forces. The measurement of rheological properties is applicable to all materials –from fluids such as dilute solutions of polymers and surfactants through to concentrated protein formulations, to semi-solids such as pastes and creams, to molten or solid polymers.

In practice, rheology is principally concerned with extending the "classical" disciplines of elasticity and Newtonian fluid mechanics to materials whose mechanical behaviour cannot be described with the classical theories. Table 3.1 helps to better understand the role of rheology in relation to mechanical behaviour of materials.

**Table 3.1** Overview of possible mechanical behaviour of matter: the role of rheology.

<b>Continuum mechanics</b>  Studies the physical behaviour of materials as continuous mass	<b>Solid mechanics</b>  Studies physics of continuous materials with a defined rest shape.	<b>Elasticity</b>  Describes materials that return to their rest shape after stress removal.	
		<b>Plasticity</b>  Describes materials that permanently deform after a sufficient applied stress	<b>Rheology</b>  Studies materials with both solid and fluid characteristics.
	<b>Fluid mechanics</b>  Studies the physics of continuous materials, which deform when subjected to a force.	<b>Non-newtonian behaviour</b>  Describes materials that have no proportional relation between shear rate and strain	
		<b>Newtonian behaviour</b>  Describes materials that undergo strain proportional to the applied shear rate.	

Rheology unites the seemingly unrelated fields of plasticity and non-Newtonian fluid dynamics by recognizing that materials undergoing these types of deformation are unable to support a stress in static equilibrium. In this sense, solids undergoing plastic deformation are fluid, although no viscosity coefficient is associated with its flow.

Polymer solutions and melts exhibit some properties that are usually associated both with solids and liquids: they are named *viscoelastic* materials.

Many commonly used materials exhibit complex rheological properties, whose viscosity and viscoelasticity can vary depending upon the external conditions applied, such as stress, strain, timescale and temperature. Internal sample variations such as protein concentration and stability, and formulation type for biopharmaceuticals, are also key factors that determine rheological properties.

In particular, a given material can behave as a solid or a liquid depending on the time scale of the deformation process; thus, in a slow flow process a material may show liquid characteristic behaviour, while it behaves like a solid when subjected to sudden deformation.

In this context, the introduction of the *Deborah number* ( $De$ ) may result a helpful concept.  $De$  is defined through the equation (3.5), where  $T$  is the characteristic time of a certain deformation process and  $\lambda$  is the relaxation time typical for each material.

$$De = \frac{\lambda}{T} \quad (3.5)$$

$\lambda$  Can be defined equal to zero for a Newtonian (purely viscous) liquid and infinite for a perfectly elastic solid.

High values of  $De$  correspond to solid-like behaviour, low Deborah numbers to liquid-like behaviour. Therefore, a material can appear liquid-like when it's deformed also if it is not when no stress is applied to it. This may occur when the characteristic time of deformation is very high, i.e. when the deformation process is very slow. On the other hand, even mobile liquid systems with very low  $\lambda$  can behave like elastic solids when exposed to a very fast deformation process.

The Deborah number concept highlights the fact that is not only the relaxation time  $\lambda$  that determines material behaviour after deformation, but also the time scale of the considered deformation process.

Rheological properties impact at all stages of material use, across multiple industries –from formulation development and stability to processing to product performance.

Rheological properties can be measured from bulk sample deformation using a mechanical rheometer, or on a micro-scale by using a microcapillary viscometer.

### 3.3.1.1 Viscosity

The viscosity is a measure that describes a fluid resistance to gradual deformation by shear stress or tensile stress; shear viscosity is the one depending on shear stress deformations and it is the more frequently used to describe fluids behaviour, since it is easier to define than tensile viscosity.

Fluids resist the relative motion of immersed object through them as well as to the motion of layers with different velocities within them. Therefore, some stress is needed to overcome the friction between layers and keep the fluid moving; for a given velocity pattern, the stress required is proportional to fluid's viscosity.

Dynamic viscosity  $\eta$  is defined as the ratio (3.6) of shear stress  $\tau$  to shear rate  $\dot{\gamma}$ ; it is measured in Pa·s.

$$\eta = \frac{\tau}{\dot{\gamma}} \quad (3.6)$$

Relation (3.6) is explained through the idealized situation on Figure 3.15, where a layer of fluid is included between two horizontal plates, one fixed and one moving horizontally at a constant speed  $v$ .

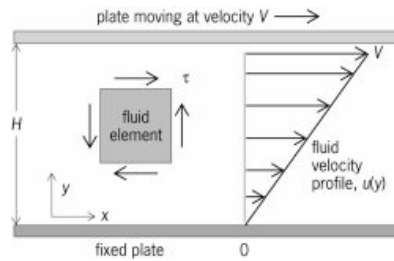


**Figure 3.15** Fluid element between a plate moving at velocity  $v$  and a fixed one: stress analysis.

If the speed of the top plate is small enough, the fluid layers will move parallel to it and their speed will decrease linearly from  $v$  at the top to zero at the bottom; friction between the layers of fluid gives rise to a force resisting their relative motion: an external force  $F$  is required to keep the top plate moving at a stationary state.

The magnitude of  $F$  defines the shear stress  $\tau$  as in (3.7), where  $A$  is the plate surface where the force is applied. The shear rate  $\dot{\gamma}$  is whereas the derivative of the fluid speed in the direction  $y$  perpendicular to plates.

$$\tau = \frac{F}{A}, \quad \dot{\gamma} = \frac{\partial v}{\partial y} \quad (3.7)$$

The equation (3.6) is often expressed as in (3.8) and in this form it is known as Newton's law of viscosity or constitutive equation.

$$\tau = \frac{\eta}{\dot{\gamma}} \quad (3.8)$$

A fluid that behaves according to Newton's law is said to be a Newtonian fluid and its viscosity is independent to the stress applied and time.

Nevertheless, most of the polymeric fluids have non-Newtonian behaviour, i.e. their viscosity is shear rate or time dependent. This rheological behaviour is well described by the equations (3.9), where  $K$  is the *consistence coefficient* and  $n$  is the index of the flux.

$$\begin{aligned}\tau &= K\dot{\gamma}^n \\ \eta &= K\dot{\gamma}^{(n-1)}\end{aligned}\quad (3.9)$$

In Figure 3.16 the various types of non-Newtonian fluids are presented.

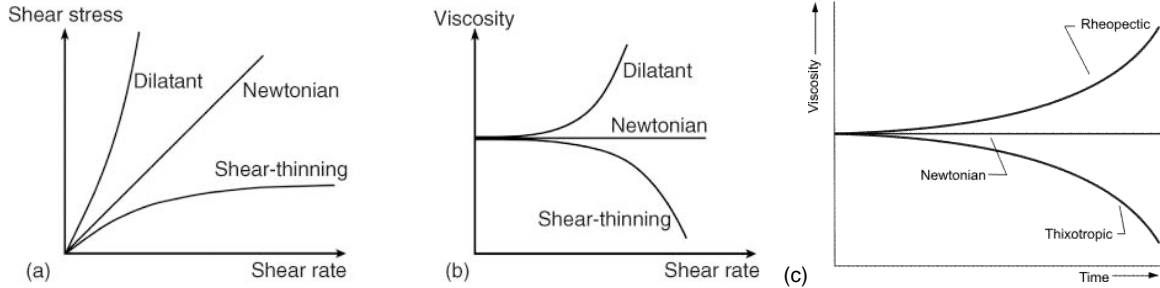


**Figure 3.16(a)-(b)** Non-Newtonian fluids with shear rate dependent viscosity. **(c)** Non-Newtonian fluids with time dependent viscosity.

In particular, a high number of melt polymers or polymer solutions are *shear-thinning*, that is their viscosity decreases for higher shear rates ( $n < 1$ ). The opposite behaviour is observed for *dilatant* fluids, which increase their viscosity when the shear rate increases ( $n > 1$ ). For Newtonian fluids, instead,  $n = 1$ .

About time-dependent behaviours, *rheopectic* fluids increase viscosity in time, while *thixotropic* fluids have the opposite trend.

### 3.3.1.2 Viscoelastic behaviour

As seen in the previous paragraph §3.3.1.1, materials may answer to mechanical loads in different way. The two main opposite types of mechanical behaviours are the elastic behaviour and the viscous one.

When an *elastic material* is deformed due to an external force, it experiences internal forces that oppose the deformation and restore it to its original state, if the external force is no longer applied; there is no energy loss during the deformation. The measure of the inherent stiffness of such a material, as a resistance to deformation under an applied load, is expressed with the elastic modulus. Actually, there are various definitions of elastic modulus in relation to the kind of deformation applied; generally, Young's modulus  $E$  is used when a tensile stress is applied while shear modulus  $G$  refers to shear stress. In Figure 3.17 a schematic representation of shear strain is reported, since it will be the one taken into account in the present study.



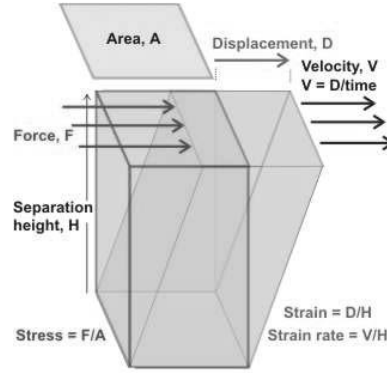


**Figure 3.17** Schematic representation of shear strain generated by a simple shear stress.

The definitions of the most important elastic moduli are reported in equations (3.10) derived from Hooke's law, where  $\sigma$  and  $\tau$  are the tensile and the shear stress and  $\varepsilon$  and  $\gamma$  are the tensile and the shear strain respectively.

$$E = \frac{\sigma}{\varepsilon}, \quad G = \frac{\tau}{\gamma} \quad (3.10)$$

On the contrary, *viscous materials* don't stretch like elastic materials when a force is applied to them, but they flow like a liquid. The behaviour of a viscous material after deformation was already described in §3.3.1.1 and it is typical of fluids.

Many real materials' can't be described with only one of these behaviours; they rather show intermediate characteristics between them. In this case, the behaviour is said to be *viscoelastic*. In viscoelastic materials the relationship between stress and strain depends on time or, in the frequency domain, on frequency.

Viscoelasticity phenomenon is studied using dynamic mechanical analysis applying a small oscillatory stress to a material and measuring the resulting strain.

In purely elastic materials the oscillatory stress and corresponding strain occur in phase, i.e. the response of one occurs simultaneously with the other. In purely viscous material, instead, there is a phase difference between stress and strain, in particular there is a lag in phase of  $\pi/2$  between stress and strain.

Therefore, viscoelastic materials exhibit behaviour somewhere in between that of purely viscous and purely elastic material, with some phase lag in strain.

For viscoelastic materials stress and strain can be represented using the sinusoidal equation in (3.11), where  $\omega = 2\pi f$ ,  $f$  is the frequency of stress and strain oscillation,  $t$  is time and  $\delta$  is the phase lag between stress and strain.

$$\begin{aligned} \varepsilon &= \varepsilon_0 \sin(t\omega) \\ \sigma &= \sigma_0 \sin(t\omega + \delta) \end{aligned} \quad (3.11)$$

In this context, it is defined a *complex shear modulus*  $G^*$  (3.12) that covers both elastic and viscous components of the material. In the same way, also a complex tensile modulus can be defined but in the present study it won't be used in the rheological analysis.

$$G^* = G' + iG'' \quad (3.12)$$

$G'$  and  $G''$  are respectively the *storage* and *loss modulus*, characteristic for viscoelastic solids,  $i$  is the imaginary number indicating that the storage modulus is “out of phase” with the loss modulus.

$G'$  measures the stored energy representing the elastic portion,  $G''$  measures the mechanical energy converted to heat through viscous frictional forces, representing the viscous portion. They are defined in relation (3.13).

$$\begin{aligned} G' &= \frac{\tau_0}{\gamma_0} \cos \delta \\ G'' &= \frac{\tau_0}{\gamma_0} \sin \delta \end{aligned} \quad (3.13)$$

For a fluid viscoelastic material  $G''$  is higher than  $G'$ , while the contrary is true for a viscoelastic solid material.

### 3.3.1.3 Rheometer geometries

A laboratory device called rheometer carries out fluid rheology investigation.

Rotational methods of measurement are usually better suited for the measurement of concentrated suspensions, gels and pastes even if less precise as compared to capillary methods.

In fact, in rotational methods the test fluid is placed between two surfaces, one or both of which are rotating, and here it is continuously sheared. The advantage of this device is that it is able to shear a sample for an unlimited period of time, permitting transient behaviours to be monitored or an equilibrium state to be achieved, under controlled rheometric conditions.

In continuous rotation testing the measurement fall into one of the following categories: *stress-controlled* and *rate-controlled*. Stress-controlled measurements consist on the application of a known stress that here is a torque, to the sample and on recording of the resultant displacement as strain or strain rate; in rate-controlled mode a defined shear rate, or rotational speed  $\omega$ , is applied and the resultant torque is measured.

Also oscillatory testing is often employed since it is an ideal technique for investigating structure and structural changes in materials. Unlike constant shear measurements, rotational testing is a non-destructive technique, involving the application of a sinusoidal oscillating stress wave to a sample and the measurement the resulting strain wave. Data of most interest derived from these oscillation strain measurements are storage and loss moduli as a function of oscillation frequency.

Many different kinds of rheometer exist and they are distinguished for the geometry of their structure. In general, the rheometer geometry is chosen according to the characteristics of the material that has to be studied.

Most rheometers depend on the relative rotation about a common axis of one of three tool geometries reported in Figure 3.18: concentric cylinders, cone and plate or parallel plates.

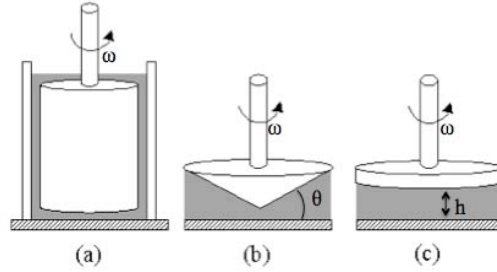


**Figure 3.18** Schematic diagram of basic tool geometries for the rotational rheometer: (a) concentric cylinder, (b) cone and plate, (c) parallel plate.

The basic rotational system consists of four parts:

- (i) A measurement tool with a well-defined geometry;
- (ii) A device to apply a constant torque or rotation speed to the tool over a wide range of shear stress or shear rate values;
- (iii) A device to determine the stress or shear rate response;
- (iv) Some means of temperature control for the test fluid and tool.

In the *concentric cylinder*, either the inner, outer or both cylinders may rotate, depending on the instrument design. The test fluid is maintained in the annulus between the cylinder surfaces. This tool geometry comes in several configurations, depending on the inner cylinder's configuration.

The *cone and plate* geometry consists of an inverted cone in near contact with a lower plate. The cone is usually designed with an angle of less than  $4^\circ$ . Either the upper or lower surface may rotate depending on instrument design.

The *parallel plate* geometry can be considered a simplified version of the cone and plate, having an angle of  $0^\circ$ . The test fluid is constrained in the narrow gap between the two surfaces.

Parallel plate measurement tools are most often used for highly viscous pastes, gels, and concentrated suspensions; while the concentric cylinder and cone-plate geometries are typically used for the analysis of fluid suspensions.

### 3.3.2 Magneto-rheological investigation: experimental conditions

In this work cone-plate geometry was employed for rheometric testing.

In this cone-plate context, the shear strain rate  $\dot{\gamma}$  is related to rotational speed  $\omega$  of the conical element by the equation (3.14), where  $\theta$  is the design angle of the cone (Figure 3.18).

$$\dot{\gamma} = \frac{\omega}{\theta} \quad (3.14)$$

The rheometer couple  $M$  instead is linked to the stress  $\tau$  according to (3.15), where  $R$  is the cone ray.

$$\tau = \frac{3M}{2\pi R^3} \quad (3.15)$$

The cone tool is placed on the superior side of the instrument and it is the only one element that rotates. Geometric characteristics of the cone are well defined:

- Diameter  $D=59.936\text{mm}$ ;
- Angle  $\theta=1^\circ$ ;
- Gap between the cone vertex and the plate during the test  $d=0.052\text{mm}$ ;
- Non-magnetic material.

For this configuration 1mL volume of material is enough to do the measurement. The sample is placed upon the fix plate, where temperature is controlled by a Peltier effect system and water circulation from a thermostatic bath at  $25.0\pm0.2^\circ\text{C}$ .

This rheometer is a stress-controlled device by Thermofisher, where an engine imposes a rotational couple to the conical tool and measures his angular speed  $\omega$ .

It is also equipped with a magnetic cell developed in the MSC laboratory, in order to execute measurements under effect of a continuous magnetic field [Ponton, 2010]. This device consists of two coils placed in both sides of the cone-plate geometry mounted on the rheometer with the bottom plate placed in the upper part of the lower coil; this configuration allows the creation of a homogenous magnetic field perpendicular to the shear stress.

### 3.3.2.1 Oscillatory measurements

Oscillatory testing was performed imposing a sinusoidal strain with constant amplitude of 1% and an oscillation frequency varying from 0.01Hz to 100Hz (low frequencies).

It was done for different magnetic field values, from  $0\text{kA}\cdot\text{m}^{-1}$  to  $31.6\text{kA}\cdot\text{m}^{-1}$ .

The storage and loss modulus where represented in relation to frequency.

### 3.3.2.2 Shear measurements

A viscosity measurement in relation to shear rate was performed, with shear rate in the range from  $10\text{s}^{-1}$  to  $2000\text{s}^{-1}$ .

This was repeated for different magnetic fields, from  $0\text{kA}\cdot\text{m}^{-1}$  to  $25\text{kA}\cdot\text{m}^{-1}$ .

### 3.3.2.3 Measurements of magnetic reversibility

Measurements of magnetic reversibility consist on two consecutive applications of shear stress under the same magnetic field. After the first measure under magnetic field, this was

turned off for a time period equal to measurement's duration. Then, another one measure was performed.

#### 3.3.2.4 Brillouin spectroscopy

Brillouin spectroscopy is a well-established optical spectroscopy technique to investigate mechanical as well as magnetic properties of matter. This technique bases on the phenomenon of inelastic laser light scattering, for which the incident photons are scattered by thermally driven elementary excitation of matter, like sound waves (acoustic phonons) or spin waves (magnons). Brillouin spectroscopy gives access to hypersonic waves and spin waves without exciting them explicitly by transducers.

Acoustic phonons study allows measuring phonons dispersion relation and thus obtaining information about materials, such as their elastic constant.

In this study, Brillouin spectroscopy was used to the aim of perform oscillatory test at very high frequencies, in the order of GHz, and then compare the results with those obtained from oscillatory test at relatively low frequencies (§3.3.2.1).

Measurements were performed whit an experimental instrument, engineered by P. Djemia in University of Paris 13 (Figure 3.19), on alginate solution with suspended DOPA NPs.

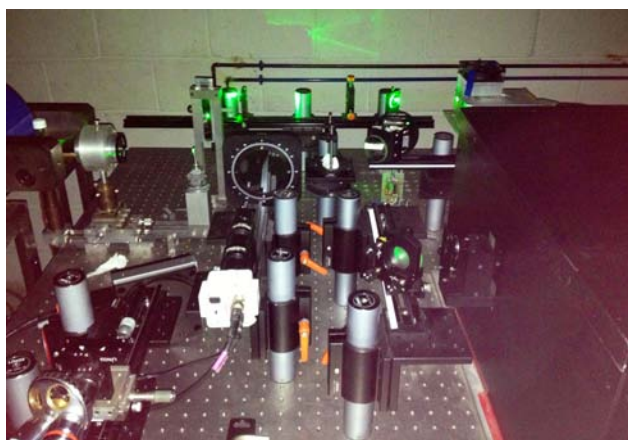


*Figure 3.19 Instrument used for Brillouin spectroscopy.*

The incident beam had wavelength of 532nm and induced oscillatory strain in alginate of about 7.8 GHz. Moreover different increasing values of magnetic field were applied during the test: 75 Gauss, 125 G, 500 G and 1000 G.

Magnetic field was applied to the sample for 10 minutes, in order to let the solution adapt itself to the field, before recording the measurement. After this, 10 minutes were waited to let the material relax its structure before applying once again the magnetic field and starting a new analysis.

### *3.3.3 Optical microscopy under magnetic field*

Optical microscopic observations were performed on sodium alginate coupled with dopamine decorated NPs, in order to investigate particles' behaviour during magnetic field application, their structuring as long as polymer reaction to magnetic field removal.

The sample was placed in a capillary tube 5cm long, 1mm wide and 0.2mm thick. Magnetic field was of  $24 \text{ kA}\cdot\text{m}^{-1}$ , orthogonal to microscope objective lens.

# Chapter 4

## Characterisation Results

### 4. 1 Bare maghemite nanoparticles

After each maghemite NPs synthesis, the product was weighted on a microbalance with  $\pm 0.01\text{mg}$  of precision. Three synthesis were effected, each of them producing about 1500mg. Since particles obtained from each synthesis showed the same results in characterizations, in this report characterization results refer to analysis carried out on samples of all obtained particles mixed together.

#### 4.1.1 IR-ATR spectroscopy

IR spectroscopy is generally used to characterise the structural type of oxides spinels, studying Fe-O bonds vibration modes, and also the state of the surface, identifying the adsorbed organic groups.

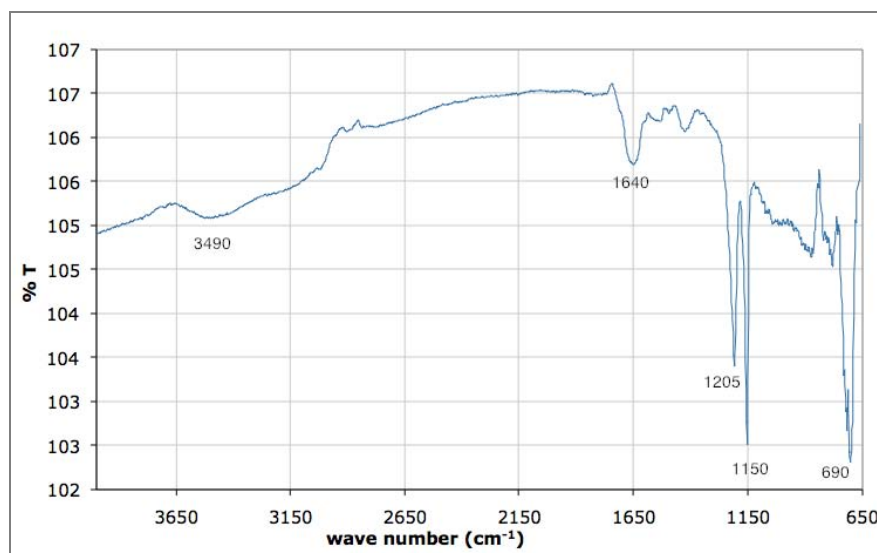


*Figure 4.1 Infra-Red spectrum of bare maghemite NPs.*

These two different kinds of information come from two different areas of spectrum: wave numbers  $\nu < 800\text{ cm}^{-1}$  give information about inorganic phase, while  $4000 < \nu < 800\text{ cm}^{-1}$  is related to superficially adsorbed species.

Results of IR spectroscopy attested maghemite phase formation and identified adsorbed species eventually present at the surface.

IR spectrum collected for bare NPs is reported in Figure 4.1, where some typical absorption bands can be seen.

Very defined peaks are recorded between  $1600\text{ cm}^{-1}$  and  $1100\text{ cm}^{-1}$  that can be attributed to residual species adsorbed on surface from the synthesis solution. Among these, the peak at  $1640\text{ cm}^{-1}$  can be attributed to symmetric and asymmetric elongational vibration of C=O functions in acetate molecules; at  $1205\text{ cm}^{-1}$  and  $1150\text{ cm}^{-1}$  instead there are two peaks due to stretching vibration of C-OH in polyol. These adsorbed species are eliminated from the surface after several washes of the particles.

On the other hand, the wide band recorded around  $3490\text{ cm}^{-1}$  belongs to hydroxyle groups on surface and it is not eliminated by NPs washes.

Finally, the peak around  $690\text{ cm}^{-1}$  is due to Fe-O bond stretching vibration, which attests the presence of an iron oxide phase and corresponds to maghemite.

In theory spinel structure presents four characteristic vibration bands relating to metal-oxygen bonds:  $\nu_1 < \nu_2 < \nu_3 < \nu_4$ . These bands are all recorded at  $\nu < 400\text{ cm}^{-1}$ , except for  $\nu_1$  that is generally associated to intrinsic vibrations of metal-oxygen bond with the metal in tetrahedral position<sup>38</sup>.

The peak recorded at  $\nu_1$  wave number is usually used to verify the oxide formation and it is the one observed also in the present spectrum. The energy and intensity of this peak depend on the cation occupying tetrahedral sites in spinel structure. A decrease of cationic ray induces an oxidation state change and the peak shift toward red wavelength<sup>39-40</sup>.

In this study, tetrahedral sites were occupied by only iron ions.

#### *4.1.2 X-Ray Diffraction*

XRD pattern recorded during maghemite NPs characterization is the one in Figure 4.2.

This pattern was compared with ideal diagrams included in the JCPDS (Joint Committee for Powder Diffraction Standard) database of Highscore software, which allowed confirming iron oxide formation with pure spinel structure.

Because of crystallographic similarity of both magnetic iron oxides, it's not possible determine with XRD analysis either maghemite or magnetite was obtained. The only one characteristic that here can distinguish the oxides is the powder colour, which is brownish rather than black and thus guarantees maghemite formation.

Diffraction diagrams were characterized by broad peaks (Figure 4.2), which generally suggest nanocrystalline character of the powder. Size estimation with Scherrer equation (3.3) confirmed this, giving a NPs mean size of about 10nm. A further validation of Scherrer size estimation was performed by TEM analysis.



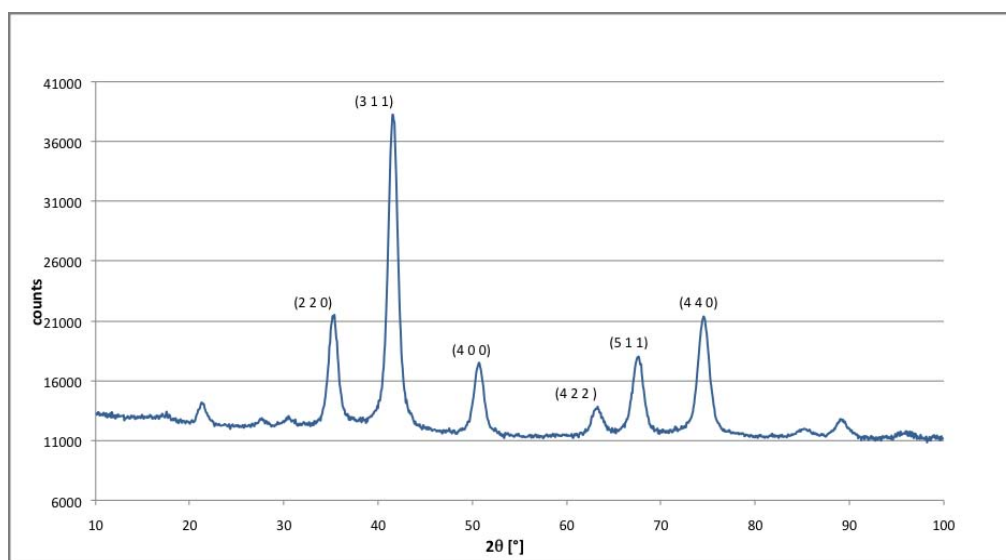


**Figure 4.2** Diffraction X diagram of bare maghemite NPs.

XRD results can be furthermore analysed using the software MAUD, in order to determine the mean size of the crystallites and the geometry of the as-produced NPs. It was found an average diameter of  $9.5 \pm 0.5\text{nm}$ ; for the calculation the peaks between  $20^\circ$  and  $30^\circ$  were excluded.

#### 4.1.3 Transmission Electron Microscopy

TEM results allowed the morphological analysis of maghemite NPs, both from the qualitative and quantitative point of view.

Several images of NPs were collected and used for the analysis; two of those are reported in Figure 4.3 as example.

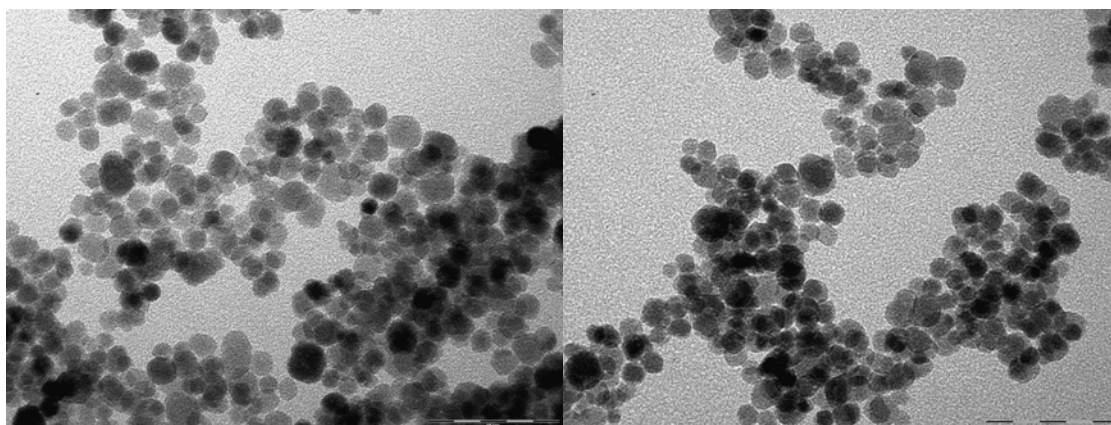


**Figure 4.3** Examples of TEM images collected for maghemite NPs. The reference line on bottom right of the images corresponds to 50nm size.

The simple observation of these images can highlight that the powder analysed was constituted by NPs of reasonably uniform size and spherical shape; the darker zones in the images are due higher concentration of the sample, derived from some unstable aggregates formation.

High resolution TEM analysis also permitted to observe high crystalline quality of NPs synthesized with the same protocol used in this work<sup>27</sup>, so it can be assumed to be the same here.

With the image analysis software SAISAM it was furthermore possible performing a quantitative study to determine the NPs mean size and their size distribution.

About 300 NPs were selected from all the collected images, their size was measured and the average size value calculated by the software. The size distribution in Figure 4.4 and an average size of 10.16 nm were observed.

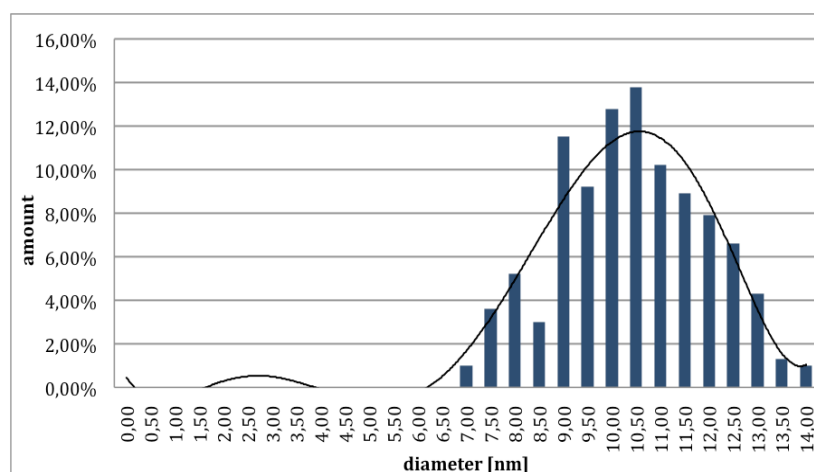


**Figure 4.4** Size distribution histogram of maghemite NPs.

In Table 4.1 various parameters carried out by image analysis are resumed.

The mean size value calculated with this technique accords with both Scherrer's and MAUD estimations (§4.1.2).

**Table 4.1** Data collected by image analysis with SAISAM.

	Diamètre [nm]
Number of values	305
Minimum value	6,6
Maximum value	13,7
Sum	3098,2
Mean value	10,2
Stardard deviation	1,5
Confidence interval	0,17

#### 4.1.4 Thermo Gravimetric Analysis

TGA was performed in air and recorded both organic and inorganic mass losses that occurred when particles were heated from room temperature (RT) till 1000°C. Moreover, DSC analysis recorded heat flow in the sample, highlighting phase transitions of iron oxide that normally change its crystalline structure when heated.

In detail, the results recorded during TGA are listed in Table 4.2. A starting mass of 29.39mg was employed for it.

**Table 4.2** TGA analysis results for bare maghemite NPs.

Starting mass [mg] = 29.39		T = room temperature	
T [°C]	30.70 → 171	171 → 643	538
Mass loss [wt%]	2.95	1.64	-
Mass loss [mg]	1.16	0.64	-
Heat flow [μV]	-	-	42.76

As it can be also seen in Figure 4.5, three different sample transformations can be located in the thermogram:

- $T \lesssim 100^{\circ}\text{C}$ , that come up to physisorbed water endothermic evaporation;
- $100^{\circ}\text{C} \lesssim T \lesssim 600^{\circ}\text{C}$  where organic chemisorbed species exothermically evaporate, among these acetate and polyol residual from synthesis process;
- $T \simeq 600^{\circ}\text{C}$  where an exothermic transition occurs, without a noticeable mass loss.

The precise ranges of temperatures where transitions occur are listed in Table 4.2.

The phase transition exothermic peak recorded at about 540°C can be attributed to maghemite  $\gamma\text{-Fe}_2\text{O}_3$  to hematite  $\alpha\text{-Fe}_2\text{O}_3$  phase transition, since this is known to occur between 540°C to 650°C<sup>41</sup>. This conclusion was also supported by the colour modification of the sample after the analysis; the red colour of powder is indeed typical of hematite.

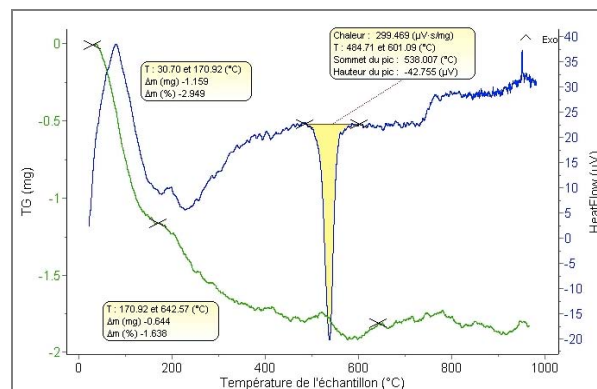


**Figure 4.5** TGA diagram: mass loss (green) and heat flow (blue) at temperature variation for bare maghemite NPs.

### 4.1.5 SQUID magnetic measurements

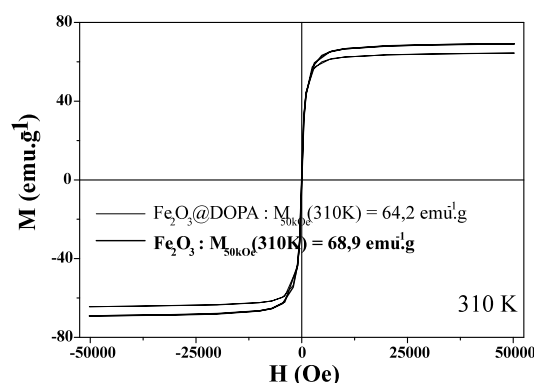


**Figure 4.6** Isotherm variation of magnetization in relation to magnetic field at 310 K for bare and dopamine grafted maghemite NPs.

Ferrimagnetic materials under their Curie temperature have typically a narrow hysteresis cycle, with a residual coercivity that is almost zero, as can be noted also in Figure 4.6.

As expected, the saturation magnetization at high magnetic field (50 Oe) is lower than that of the bulk maghemite because of NPs finite size, but they can be as well considered closed together ( $69 \text{ emu}\cdot\text{g}^{-1}$  for the NPs and  $85 \text{ emu}\cdot\text{g}^{-1}$  for the bulk maghemite).

The same type of measurement on dopamine decorated NPs highlighted that the organic matter (dopamine) is diamagnetic and its presence decrease grafted NPs saturation magnetization of about 6.8% compared to that of bare NPs.

In conclusion, the saturation magnetization of as prepared and functionalized NPs are very close together, as well as very close to that of the bulk.

## 4.2 Decorated nanoparticles

### 4.2.1 IR-ATR Spectroscopy

#### 4.2.1.1 Dopamine nanoparticles

Dopamine NPs' IR spectrum is presented in Figure 4.8, together with the dopamine one as reference.

Comparing the spectrum of decorated NPs with the one of bare NPs (Figure 4.1), some additional peaks are noticed. These peaks are recorded also in pure dopamine spectrum and thus they can be attribute to dopamine presence on NP surface. Figure 4.7 may help to better understand the vibrational modes of molecular bonds described here hereunder.

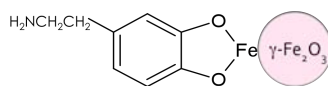


**Figure 4.7** Schematic representation of a dopamine grafted NP (DOPA NP).

The broad peak centred at about  $3400\text{ cm}^{-1}$  describes  $\text{-OH}$  groups on NPs surface due to water adsorption.

Three main peaks were used to confirm dopamine grafting; those are encircled in Figure 4.8.

In detail, absorption peak at  $\nu \simeq 1498\text{ cm}^{-1}$  are due to symmetric and asymmetric stretching vibrations of  $\text{C}=\text{C}$  bonds in the dopamine aromatic cycle. The peak at  $\nu \simeq 1269\text{ cm}^{-1}$  is related to stretching vibration of  $\text{C-O}$  bonds between the aromatic cycle and the hydroxide groups and finally, the peak at  $\nu \simeq 790\text{ cm}^{-1}$  derives from  $\text{Fe-O}$  bond stretching mode.

Other dopamine characteristic peaks are those around  $\nu \simeq 3340\text{-}3200\text{ cm}^{-1}$  due to  $\text{NH}_2$  symmetric and asymmetric stretching and at  $\nu \simeq 1620\text{ cm}^{-1}$ , due to scissoring vibration of  $\text{NH}_2$  in aromatic amines; finally, the peaks at  $\nu \simeq 1290\text{ cm}^{-1}$  and  $\nu \simeq 1190\text{ cm}^{-1}$  that are due to rocking and twisting vibration of  $\text{C-N}$  bond in aromatic amines.

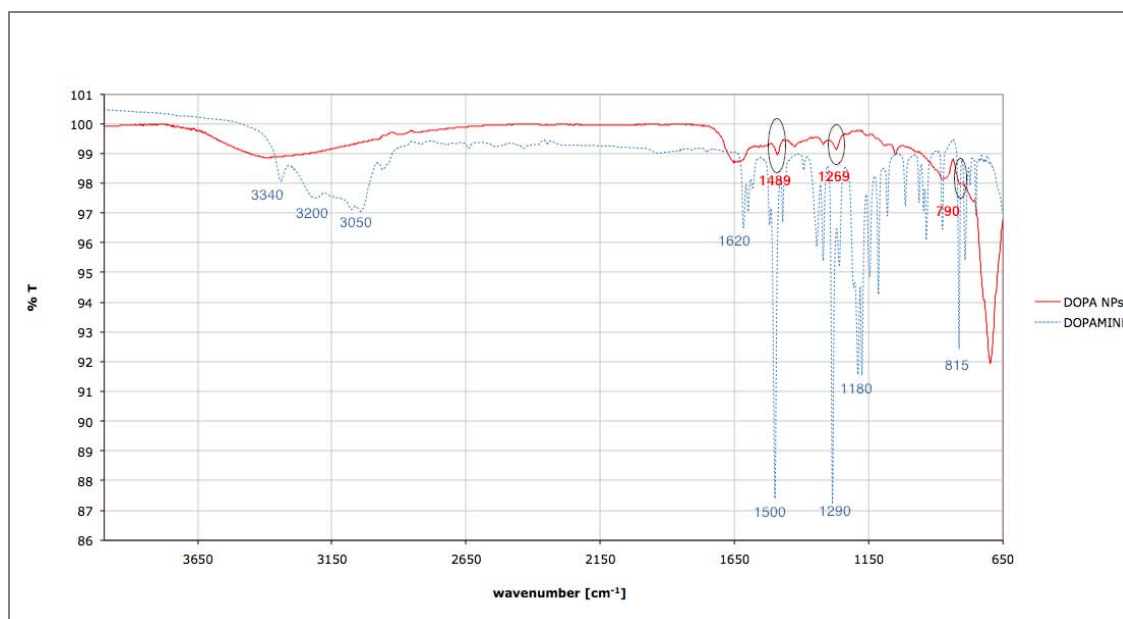


**Figure 4.8** IR spectra for dopamine (blue) and dopamine-decorated maghemite NPs (red). The main peaks wavenumbers are reported.

#### 4.2.1.2 Amino-silane nanoparticles

IR spectra of APTES grafted NPs and pure APTES are presented in Figure 4.9. Compared with bare NPs, in APTES NPs spectrum novel peaks are observed; those encircled in black were used as reference to confirm APTES grafting effectiveness.

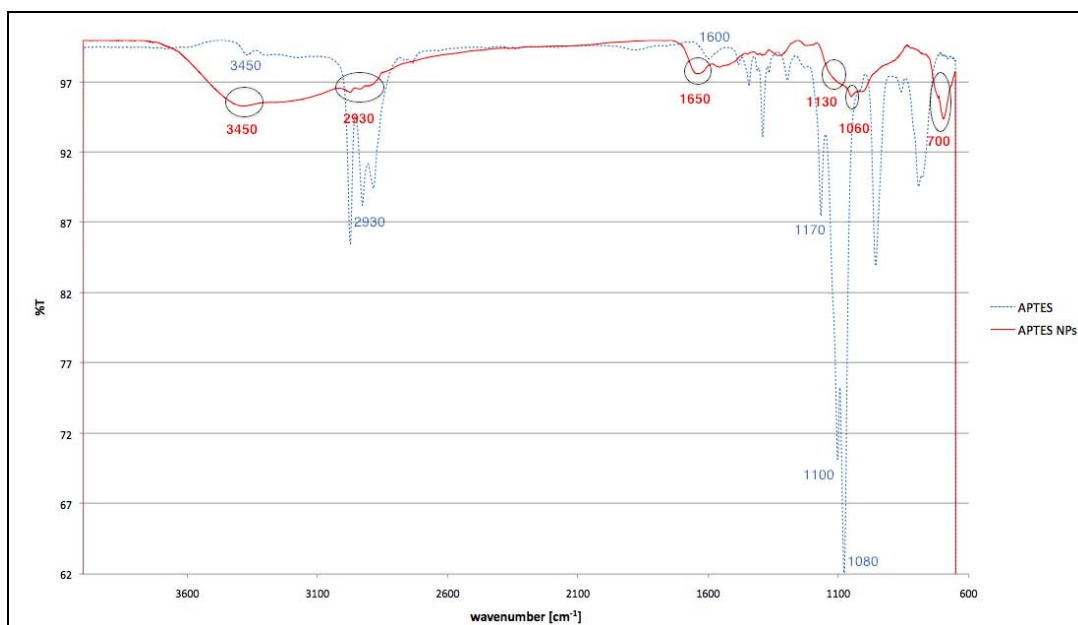


**Figure 4.9** IR spectra for APTES (blue) and APTES-decorated maghemite NPs (red). The main peaks wavenumbers are reported.

In detail, the broad peak around  $\nu \simeq 3450 \text{ cm}^{-1}$  can be associated both with -OH groups vibration and -NH stretching vibration<sup>42</sup>. The peaks around  $\nu \simeq 2930 \text{ cm}^{-1}$  are corresponding to aliphatic -CH stretching, while that at  $\nu \simeq 1650 \text{ cm}^{-1}$  to symmetric and asymmetric stretching of C=O maybe of residual acetate. The characteristic peaks of Si-O are generally difficult to recognize because they are extended in a complex spectral region characterised by a broad absorption at  $\nu \simeq 1000\text{--}1260 \text{ cm}^{-1}$  that overlaps to other absorption bands<sup>43</sup>. Two peaks at about  $\nu \simeq 1130 \text{ cm}^{-1}$  and  $\nu \simeq 1060 \text{ cm}^{-1}$  were assigned to Si-O bond, while the peak centred at  $\nu \simeq 1080 \text{ cm}^{-1}$  relates to C-O vibration modes. Finally the peak at about  $\nu \simeq 700 \text{ cm}^{-1}$  describes Fe-O stretching vibration. In Figure 4.10 a schematic representation of an APTES NP is reported, in order to better understand the bonds involved in energy absorption during IR spectroscopy.

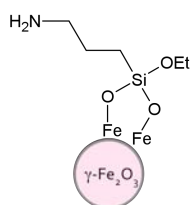


**Figure 4.10** Schematic representation of an APTES grafted NP (APTES NP).

#### 4.2.1.3 Amino-phosphonic acid nanoparticles

In Figure 4.11 PHOSP NPs and aminophosphonic acid spectra are reported.

The new peaks assigned to aminophosphonic acid grafting are encircled on PHOSP NPs spectrum.

In aminophosphonic acid spectrum, the absorption band between  $\nu \simeq 2500\text{cm}^{-1}$  and  $2800\text{cm}^{-1}$  is associated to O=PO- group vibration. Another characteristic peak is the one at  $\nu \simeq 1242\text{cm}^{-1}$  that is associated to P=O stirring vibration. Peaks around  $950\text{ cm}^{-1}$  instead are generally associated to -POR stirring vibration.

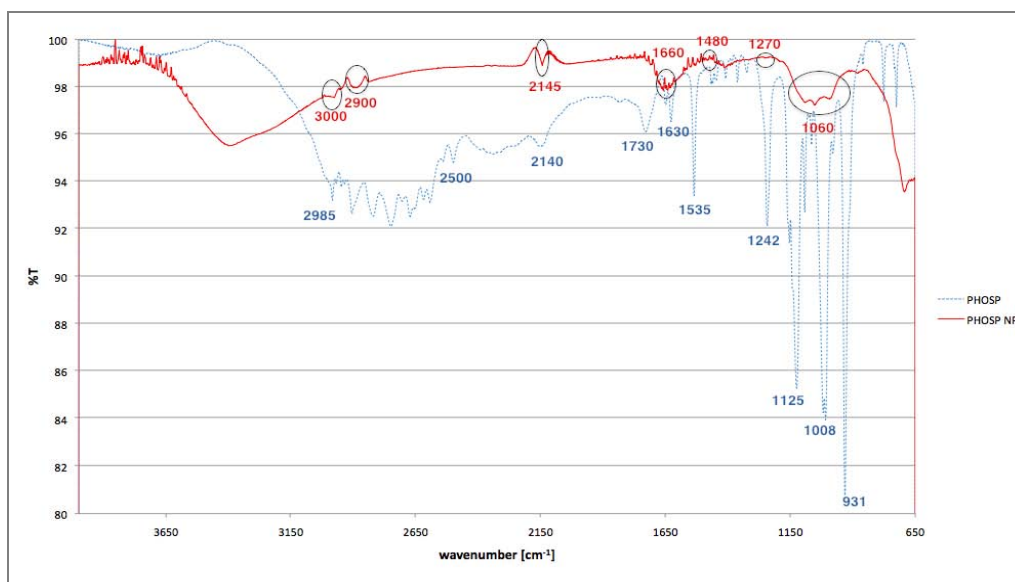


**Figure 4.11** IR spectra for 3-aminopropyl phosphonic acid (blue) and amino phosphonic acid-decorated maghemite NPs (red). The main peaks wavenumbers are reported.

## 4.2.2 Thermo Gravimetric Analysis

### 4.2.2.1 Dopamine nanoparticles

TGA results for dopamine grafted NPs are presented in Table 4.3. The three zones noted for bare NPs can be distinguished also in DOPA NPs thermogram in Figure 4.12. In addition, an exothermic peak centred at  $261^{\circ}\text{C}$  was recorded in the present result, at the same temperature where organic mass loss occurs. This exothermic heat flow means that organic species desorption release energy, thus confirming that covalent bond was broken between dopamine and NP surface.

**Table 4.3** TGA analysis results for dopamine-decorated NPs.

Starting mass [mg] = 17.58		T = room temperature		
T [°C]	28 → 178	178 → 338	261	521
Mass loss [%]	2.63	1.64	-	-
Mass loss [mg]	0.46	0.29	-	-
Heat flow [μV]	-	-	19.01	14.08

Before starting dopamine mass content on grafted NPs surface calculation, it must be reminded IR spectroscopy results, which revealed organic matter residual from synthesis solution on NPs; this organic matter is identified mainly on chemisorbed acetate that can form a complex with iron ions by mean of carboxylic groups. Therefore, dopamine grafting may occur by acetate substitution or by addition to free sites on surface.

**Table 4.4** Comparison between organic species mass loss in bare NPs and in DOPA NPs.

	NPs	DOPA NPs
<b>Organic mass loss [wt%]</b>	1.64	1.64
<b>Starting mass [mg]</b>	29.39	17.58
<b>DOPA mass content [wt%]</b>	-	0÷1.64

In this contest, dopamine mass content calculation from mass loss of organic species is executed on the basis of two different hypothesis: that dopamine is grafted to NP substituting residual acetate or that dopamine is grafted occupying free sites on NP surface. In the first case, the organic mass loss in DOPA NPs must be subtracted with organic mass loss in bare NPs. In the second case, instead, the mass loss recorded is directly equal to mass content of grafted dopamine. In Table 4.4 the dopamine mass content is estimated considering both these situation.

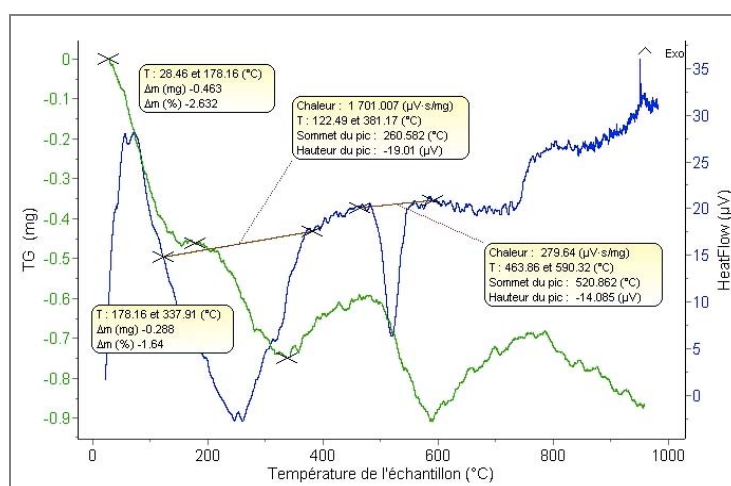


**Figure 4.12** TGA diagram: mass loss (green) and heat flow (blue) at temperature variation for dopamine decorated maghemite NPs.

Maghemite to hematite phase transformation, corresponding to DSC exothermic peak at about 540°C, is here coupled with a mass loss related to CO<sub>2</sub> evaporation after heating organic species.

Finally, on hybrid NPs was observed a dopamine mass content of about 1.6%.



#### 4.2.2.2 Amino-silane nanoparticles

Table 4.5 presents TGA results for APTES grafted NPs. Inorganic and organic species desorption are recorded at  $T \lesssim 100^\circ\text{C}$  and  $100^\circ \lesssim T \lesssim 600^\circ\text{C}$  respectively, while exothermic peaks are recorded at about  $300^\circ\text{C}$  and  $700^\circ\text{C}$ . TGA diagram is presented in Figure 4.13.

**Table 4.5** TGA analysis results for APTES-decorated NPs.

Starting mass [mg] = 14.27		T = room temperature		
T [ $^\circ\text{C}$ ]	32 $\rightarrow$ 132	271 $\rightarrow$ 591	266	731
Mass loss [%]	2.69	5.67	-	-
Mass loss [mg]	0.38	0.81	-	-
Heat flow [ $\mu\text{V}$ ]	-	-	43.73	4.39

Like dopamine mass content, also grafted APTES mass content is estimated starting from the same hypothesis, i.e. that APTES can be substituted to acetate or added on free sites upon maghemite NPs surface. The grafted APTES mass content is estimated to be between 4.03% and 5.67% of the starting mass (Table 4.6).

**Table 4.6** Comparison between organic species mass loss in bare NPs and in APTES NPs.

	NPs	APTES NPs
Starting mass [mg]	29.39	14.27
Organic mass loss [wt%]	1.64	5.67
APTES mass content [wt%]	-	4.3÷5.7

The exothermic peak at about  $700^\circ\text{C}$  corresponds to maghemite to hematite phase transition and it is accompanied by  $\text{CO}_2$  liberation from heated organic molecules.

The other exothermic peak at about  $300^\circ\text{C}$  instead confirms that the bond between APTES and maghemite NP is a strong bond that releases energy when it is broken.

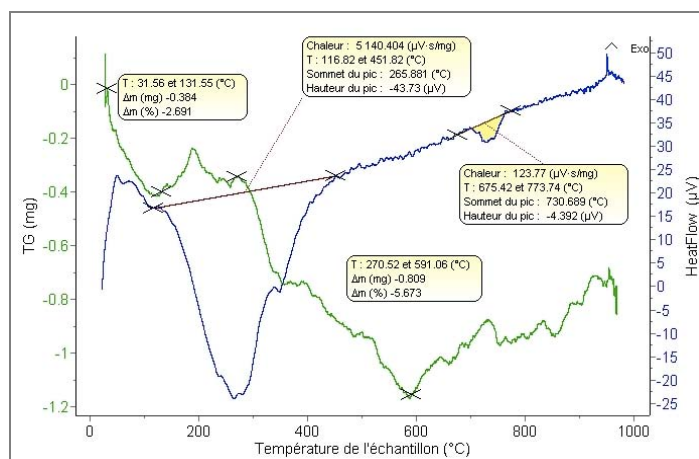


**Figure 4.13** TGA diagram: mass loss (green) and heat flow (blue) at temperature variation for APTES decorated maghemite NPs.

#### 4.2.2.3 Amino-phosphonic acid nanoparticles

Like for the other decorated NPs, TGA results are listed in Table 4.7, while the thermogram is reported in Figure 4.14.

**Table 4.7** TGA analysis results for PHOSP-decorated NPs.

Starting mass [mg] = 22.77	T = room temperature		
T [°C]	24 → 432	275	664
Mass loss [%]	5.73	-	-
Mass loss [mg]	1.31	-	-
Heat flow [μV]	--	40.16	22.72

Grafted PHOSP mass content was calculated with the same hypothesis already exposed for DOPA NPs and APTES NPs and it was supposed to be between 4% and 5.7% of the starting mass. The values used for the calculation and the results are reported in Table 4.8.

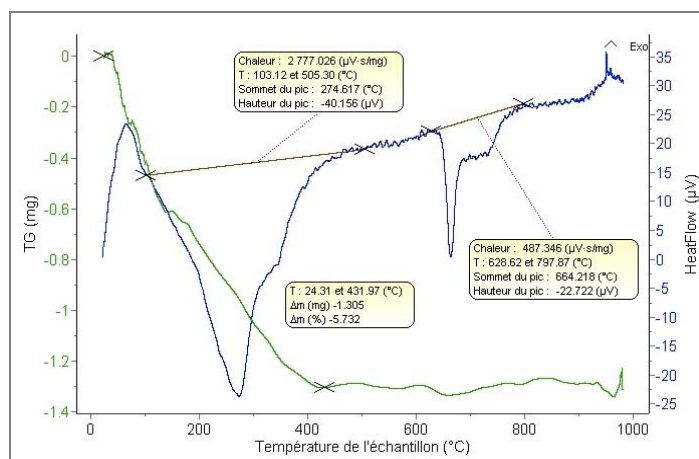


**Figure 4.14** TGA diagram: mass loss (green) and heat flow (blue) at temperature variation for PHOSP decorated maghemite NPs

**Table 4.8** Comparison between organic species mass loss in bare NPs and in PHOSP NPs.

	NPs	PHOSP NPs
Starting mass [mg]	29.39	22.77
Organic mass loss [wt%]	1.64	5.73
PHOSP mass content [wt%]	-	4.1-5.7

### 4.2.3 Stability valuation by Zeta Potential analysis

Figure 4.15 reports the average  $\zeta$ -potential calculated from three values recorded during the measurements at each pH and for each type of NPs. Also the standard deviation  $\Delta\zeta$  of each  $\zeta$  value was calculated as the average of the three measurements'  $\Delta\zeta$ .

It must be pointed out that at extreme pH values, i.e. at  $\text{pH} < 3$  and  $\text{pH} > 12$ ,  $\zeta$ -potential measurements are not reliable, since the high concentration of charge carriers in solution confuse software data elaboration.

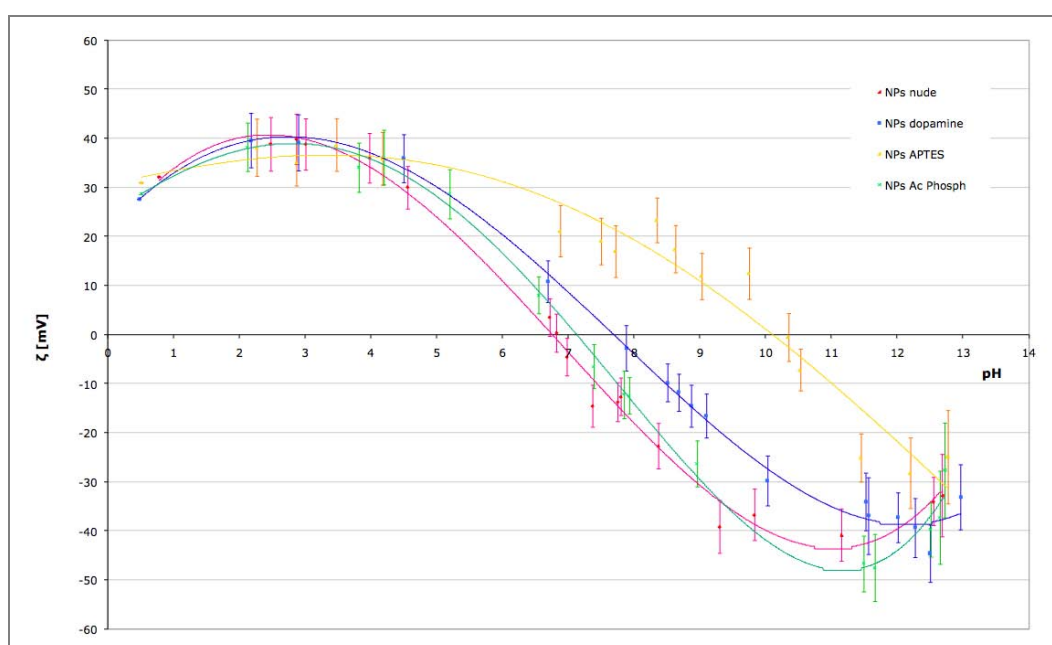


**Figure 4.15** Zeta potential pattern in relation to pH value of the environment for differently decorated NPs.

The pH range of interest is that around  $\text{pH}=7$  that is the characteristic pH of the environments where the prepared NPs will be introduced for applications; this pH range corresponds to physiological pH and also to alginate characteristic pH.

Around this pH value, the isoelectric point (IEP) of bare NPs was recorded; this means that in such environments bare NPs have no charge upon their surface and so they are unstable and sensitive to aggregation. Decorated NPs were expected to overcome this problem,

because of positively charged groups grafted on their surface. In fact for all decorated NPs, positive values of  $\zeta$ -potential were recorded around physiological pH; positive value of  $\zeta$  means that the surface of the analysed particles is positively charged. The higher is the  $\zeta$  potential, the higher the charge density on surface.

APTES NPs are those with higher  $\zeta$  values and thus the more stable, since a higher repulsion force is established between the particles in suspension.  $\zeta$  Value for DOPA NPs is a little bit lower and so they will be less stable in suspension than APTES NPs, but more stable than PHOSP NPs that exhibit the less  $\zeta$  value of all three decorated NPs.

Particles with higher charge density on surface have the IEP at more basic pH values, i.e. at higher pH.

### 4.3 FITC labelled nanoparticles

#### 4.3.1 UV-Vis spectroscopy

In UV-Vis absorption analysis the peak recorded at  $\lambda=495\text{ nm}$  was studied since it is the FITC characteristic absorption peak.

UV-Vis absorption spectra recorded are presented in Figure 4.16, while the detailed peaks of each labelling solution and the detailed peaks of each washing solutions can be observed in Figure 4.17 and 4.18 respectively.

Going from labelling solution spectra to those of washing solutions, a significant decrease of the absorption peak appears, because of the obvious lower FITC content.

Detailed peaks' images show that their intensity is different for each considered solution, higher for APTES solution, medium for PHOSP solution and lower for DOPA solution in Figure 4.17.

In Figure 4.18, instead, the intensity is higher for APTES again, but it is medium in DOPA and lowers for PHOSP solution, also if the difference between the last two solutions is little.

Higher peak intensity corresponds to higher FITC concentration in solution, according to Lambert-Beer law (3.4), and thus higher peak intensity also corresponds to lower amount of FITC grafted or adsorbed onto NPs surface.

In this contest it was supposed that FITC labelling succeeded most on DOPA NPs and then on PHOSP NPs and APTES respectively.

On the other hand, FITC grafting stability seemed to be better for PHOSP NPs and then for DOPA NPs and APTES NPs respectively.

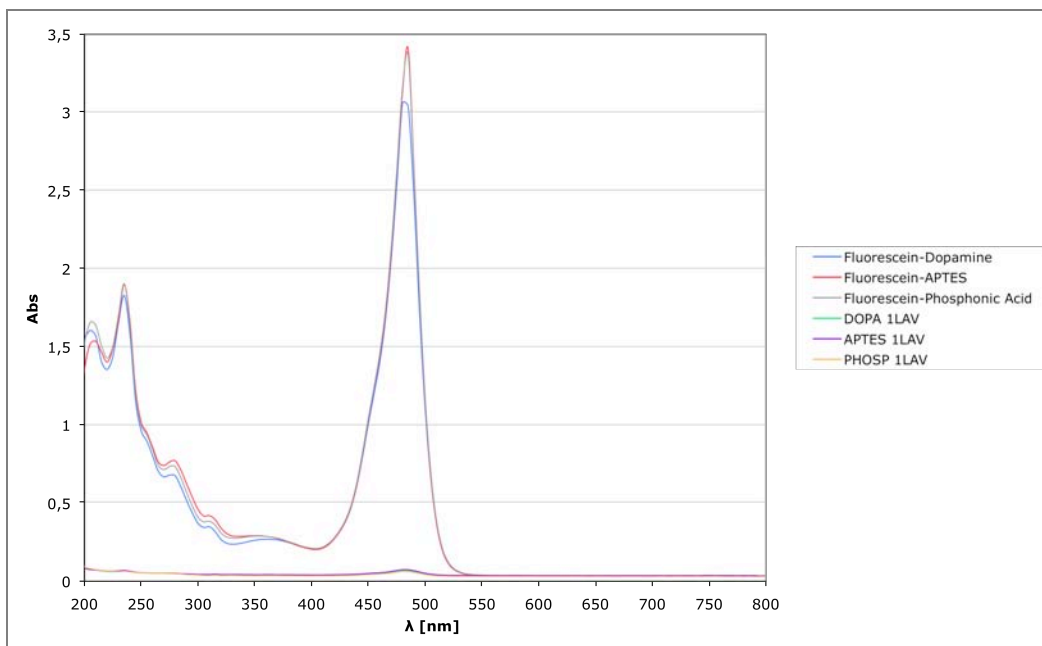


**Figure 4.16** UV-Vis spectra for FITC labeling solutions of three differently decorated NPs as obtained after labeling and after the first washing cycle.

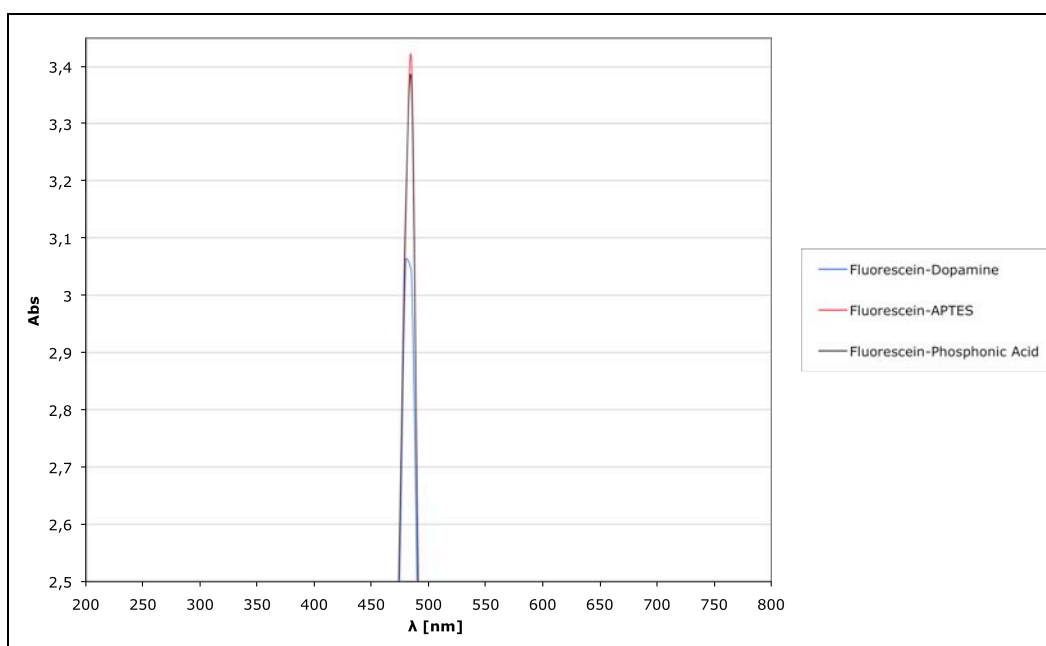


**Figure 4.17** Detail of UV-Vis spectra for FITC labeling solutions as-obtained: different intensities of FITC absorbance peak in relation to the ligand on NPs surface.

Absorption spectra of washing solutions following the first one are not reported, since their line pattern is completely flat and no peaks were recorded. This result means that after the first ultrasonic washing cycle all FITC molecules weakly bonded onto NPs surface are removed. After this, the ultrasounds energy is no longer enough to detach FITC molecules

from NPs and the remaining FITC molecules are supposed to be covalently bonded to their surface.

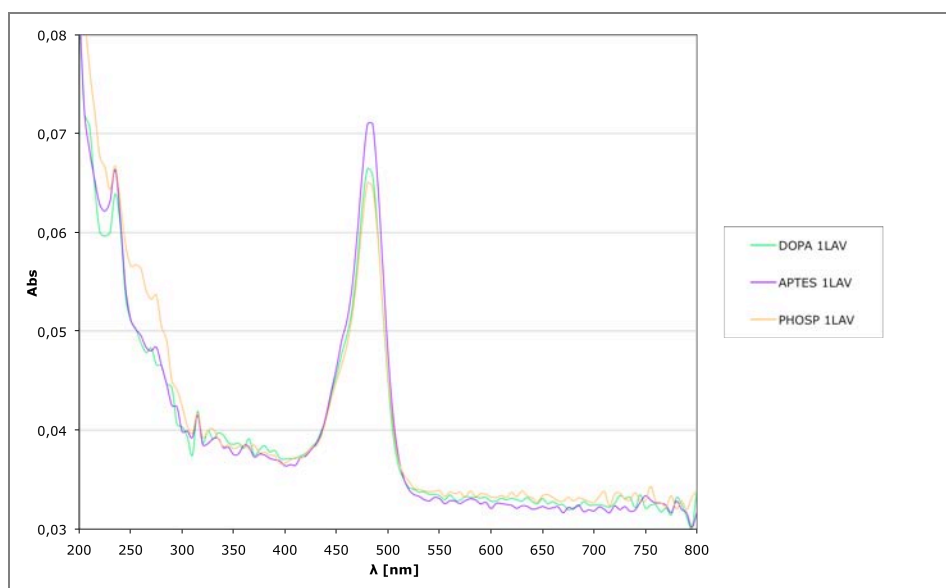


**Figure 4.18** Detail of UV-Vis Spectra for FITC NPs washing solutions.

So far, only qualitative remarks have been presented since quantitative information was deduced from absorption spectra after a calibration line calculation.

This line was obtained measuring the absorption peak intensity of three FITC solutions at known concentrations. In this way, it was possible correlating peak intensity to FITC concentration for the various considered solutions.

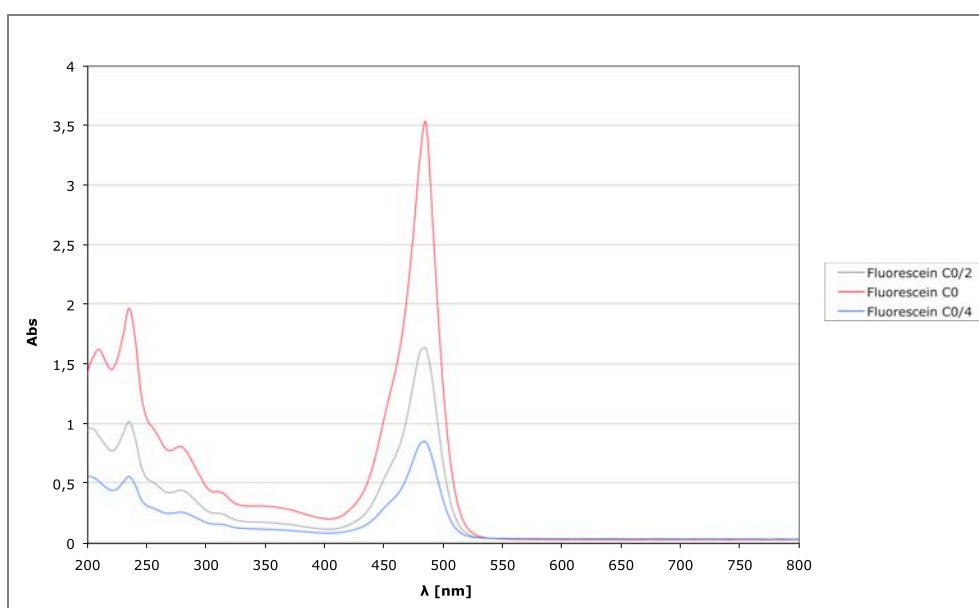


**Figure 4.19** UV-Vis absorbance spectra for FITC solutions at different concentrations.

In Figure 4.19 the absorption spectra recorded for solutions at known concentration are presented.  $C_0$  is the FITC concentration of the starting labelling solution (before introducing NPs), while  $C_0/2$  is the half value and  $C_0/4$  is a quarter of it.

The calibration line obtained from these values is represented in Figure 4.20.

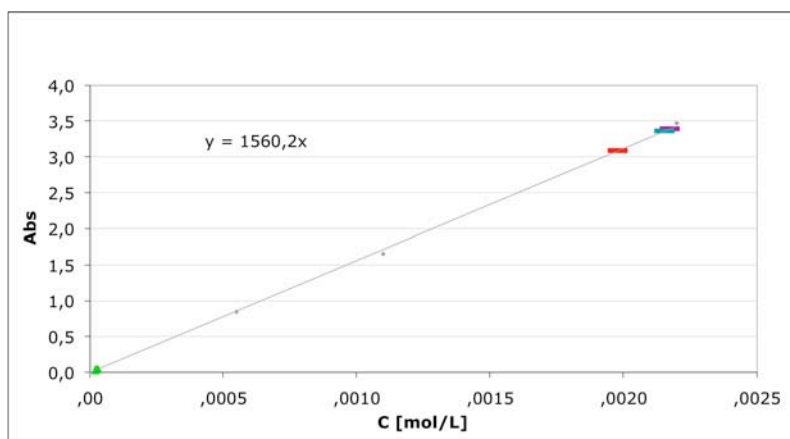


**Figure 4.20** Concentration of FITC in labeling solutions: the red mark is for DOPA NPs, the green one for PHOSP NPs and the purple for APTES NPs. The little green triangles on bottom left mark the FITC concentration in washing solutions of all three types NPs.

Using this, it was possible calculating the FITC concentration of labelling solutions for each NPs type. Here it can be seen that FITC concentration in DOPA NPs labelling solution is notably lower than the other, while a little difference is seen between PHOSP NPs and APTES NPs labelling solutions.

Moreover, the concentration of washing solutions was calculated in the same way and it was found to be almost zero for all three decorated NPs.

### 4.3.2 Calculation of FITC grafted amount

From the concentrations calculated with the calibration line in Figure 4.20, it was possible deriving the amount of FITC effectively grafted onto NPs, since after the first washing cycle no other FITC molecules detached from them.

**Table 4.9** Number of FITC molecules grafted on each NP surface, for all decorated NPs used.

	FITC molecules/NP	FITC grafting yield
DOPA NPs	8.26	9.3%
PHOSP NPs	1.41	1.6%
APTES NPs	0.40	0.45%

The concentration of grafted FITC  $C_{gr}$  on each NPs type was calculated with (4.1), where  $C_0$  is the concentration of FITC in the starting solution,  $C_{lab}$  the concentration in the labelling solution and  $C_{wash}$  the concentration of washing solution.

$$C_{gr} = C_0 - 2C_{lab} - C_{wash} \quad (4.1)$$

$C_{lab}$  is doubled, since labelling solutions was diluted before the analysis and so the effective amount of FITC contained is double compared to that calculated in Figure 4.20.

The number of FITC molecules grafted upon each NP and the yield of FITC in grafting are estimated in Table 4.9.

As observed from UV-Vis spectra analysis, the more effective ligand in grafting FITC molecules is the dopamine and moreover the number of FITC molecules per DOPA NPs calculated is in line with the amount of fluorophore molecules obtained in other successful grafting works<sup>44, 45</sup>.

## 4.4 Alginate-based nanocomposites

### 4.4.1 Oscillatory measurements

The frequency dependence of elastic and loss moduli to the applied magnetic field, at constant strain in the viscoelastic domain, was observed from the results presented in Figure 4.21. It confirms the enhancement of mechanic properties by increasing magnetic field strength until around 100Hz, above which all the curves superpose. It can be pointed out that magnetic field intensity has a significant bearing on  $G'$  and  $G''$  values and further that magnetic field effect is more conspicuous at low oscillation frequencies.

Compared to previous results obtained on alginate | 1% APTES NPs hybrids, where curves superposed at about 5 Hz frequency, in this study the curves superpose at higher frequency values.

A critical frequency can be defined by the crossover of the elastic and loss moduli curves at each magnetic field strength, which expresses the material transition from a viscous to an elastic solid condition. Figure 4.22 highlights that magnetic field strength determines the critical transition frequency and the higher the magnetic field is, the higher will be the transition frequency.

This transition frequency corresponds to the inverse ratio of relaxation time and thus increasing the magnetic field strength the relaxation time becomes lower and the material structuring faster.



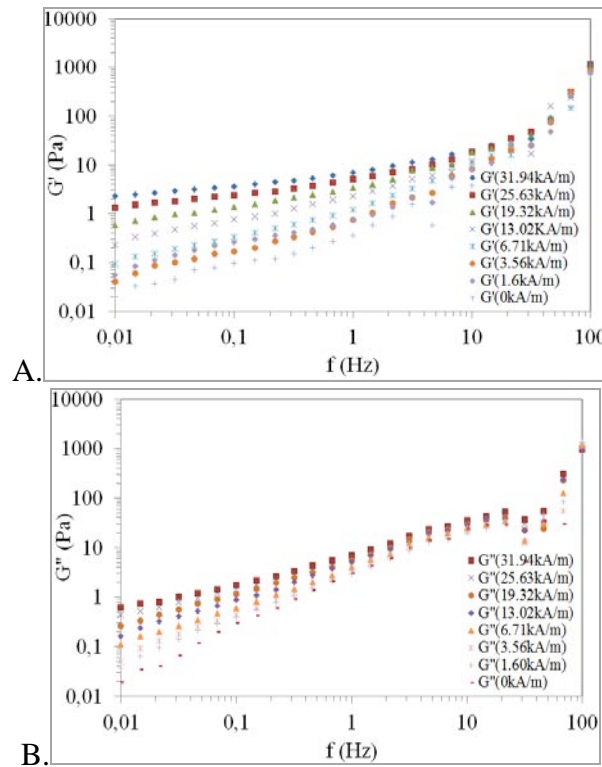


**Figure 4.21.** **A.**  $G'$  related to oscillation frequency for an alginate solution of 18g/L and 0.5% vol. of DOPA NPs; **B.**  $G''$  related to oscillation frequency for an alginate solution of 18g/L and 0.5% vol. of DOPA NPs.

The oscillatory testing performed at ultra-high frequency by Brillouin spectroscopy didn't furnish significant results, since the magnetic field applied during the measurements displaced NPs creating an homogeneous alginate solution where the sample was hit by the beam and a separated layer of NPs to the cell walls.

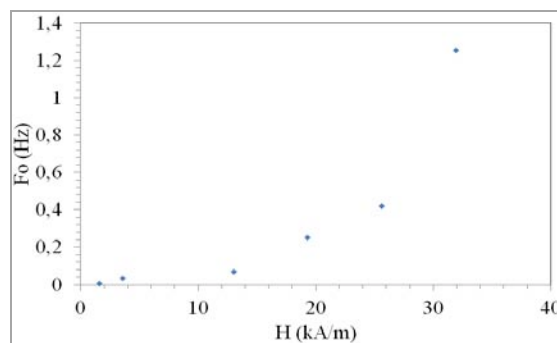


**Figure 4.22** Critical transition frequency of alginate /DOPA NPs hybrid in relation to the applied magnetic field.

So the spectra recorded for the only alginate and for the hybrid material appeared the same because in both cases they related to the alginate solution without NPs. Being a very complex analysis technique, the parameter of testing must be further tuned in order to reach a successful analysis.

#### 4.4.2 Shear measurements

Shear measurements were performed at four different magnetic field strengths between 0 and 25 kA/m, in order to observe strain rate influence on viscosity under magnetic field. These measures consist in destructive analysis, so each sample taking served a single measure recording.

It was found that viscosity increases with the magnetic field, in a more pronounced way at lower strain rate (Figure 4.23). This result can be explained by the fact that at low strain rate the magnetic field strength prevails on mechanic stresses, structuring the material. At high shear rate, instead, mechanic stresses overcome magnetic field structuring, which has no longer effects on material.

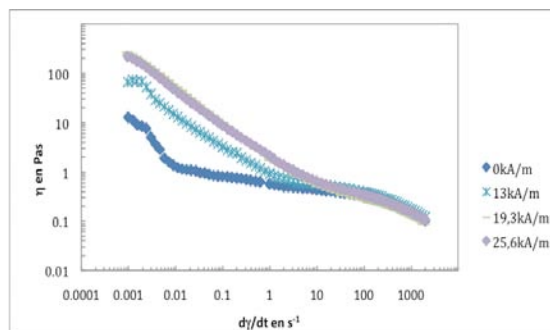


**Figure 4.23** Viscosity to shear rate diagram for an 18g/L alginate solution with 0.5%V of DOPA NPs, at various magnetic field values.

#### 4.4.3 Magnetic reversibility measurements

The magnetic reversibility was investigated for a 6.7 kA/m, 19 kA/m and 31.9 kA/m magnetic field on the alginate|0.5%DOPA NPs hybrid. For example, the 6.7 kA/m magnetic field had been switched off for 74 minutes before starting a second one measurement under the same magnetic strength. The results are reported in Figure 4.24 and they show two superposing curves for both the measurements, attesting the magnetic reversibility of such a hybrid. Thus it can be stated that the magnetic field does not alter the material in an irreversible way.

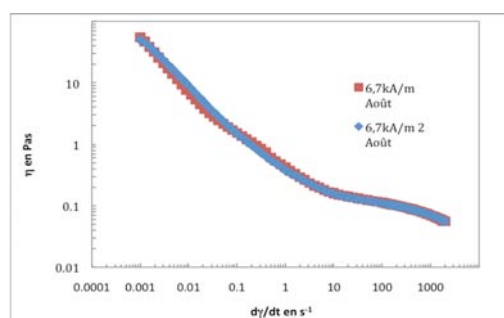


**Figure 4.24** Magnetic reversibility results with 6.7kA/m magnetic field for an 18g/L alginate solution with 0.5%V of DOPA NPs, at various magnetic field values.

#### 4.4.4 Optical microscopy under magnetic field

The images recorded at constant time intervals are presented in Figure 4.25, where the material structuring parallel to magnetic field direction is observed, after the aggregate and NPs migration and a fibrous structure formation. This structure defines itself step by step in time till the image at 120 minutes, where equilibrium seems to be reached.

At magnetic field switching-off time, parallel structures start rippling soon. For this reason NPs are assumed being fixed to alginate chain only under the magnetic field effect but they do not prevent alginate chain relaxation when magnetic field is switched-off: alginate chains entangle each other in a random way.

The only difference with the starting condition is that NPs are no longer homogeneously dispersed in the alginate solution but they stay around the polymer chains. Anyway, if a magnetic field is later applied, the fibrous structure observed in the image at 120 minutes is again recorded, so that the magnetic reversibility stated in §4.4.3 is confirmed.

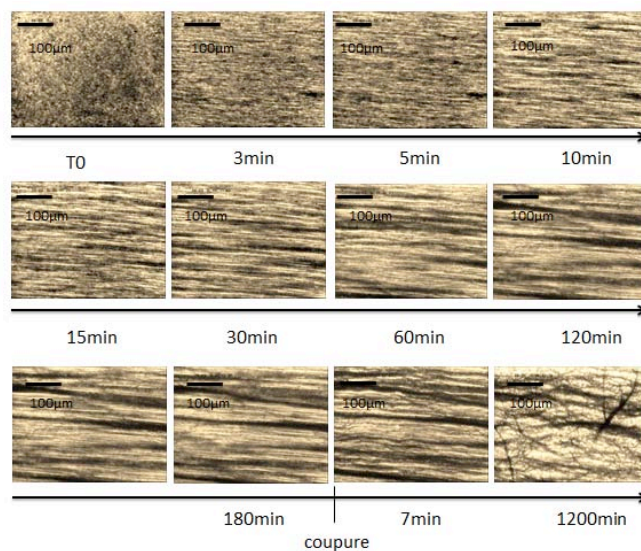


**Figure 4.25** Optical microscopy observation of the alginate solution of 18g/L with 0.5% vol. of DOPA NPs, under a 24kA/m magnetic field. The magnetic field's switch off is after 180 minutes from the beginning of observation (T0).



# Chapter 5

## Future Developments

The research just exposed has an interdisciplinary nature that range from physics, chemistry and mechanical investigation of both the hybrid material assembled and its constituting elements. For this reason the project offers various opportunities of further development that will be briefly presented in the following chapter.

### 5.1 Functional groups for NPs grafting

The overall results of characterization suggest that the ligand that best suit the expectations is the dopamine, since it seems to be the most effective in drug attachment and in the same time it has reasonable stability in solution at pH=7. Nevertheless dopamine is known to be sensitive to oxidizing agents, high temperatures and extreme pH; thus, the real application of a hybrid system containing dopamine should be further investigated as regard the ligand stability.

At the other hand, APTES and PHOSP ligands seemed to be no efficient in drug attachment. For these reason, all the ligands taken into account in this research don't fulfil completely the desired characteristics.

In order to confirm the results obtained, it would be appropriate repeating the FITC labelling, changing for example the protocol, and verifying the various ligand efficiency.

Moreover other ligand could be considered for NPs grafting and analysed with the same techniques.

Also nanoparticles grafted with a diazonium salt were taken into account in the present work and were labelled with FITC using the same protocol described in §2.3.2. No results were obtained since a too little quantity of diazonium grafted NPs was available at the moment to succeed FITC labelling; anyway, it would be interesting to continue investigating the properties of diazonium grafted NPs.

Like diazonium, other groups bearing amine function and able to complex iron oxide NPs can be researched.

Another functional group of interest could be the citrate one, since it is known than iron oxide NPs are stabilized in aqueous media at pH  $\simeq$  7 by a citrate coating<sup>45</sup>. Unlike the other studied ligands, citrate determines a negative charge on NPs surface (Figure 5.1) but it can

anyway bond a fluorophore molecule with an amine function (like fluoresceine or rodamine).

Inside the alginate network, citrate grafted NPs won't be able to establish electrostatic interactions with the chains, but they will be simply trapped between their entanglements.

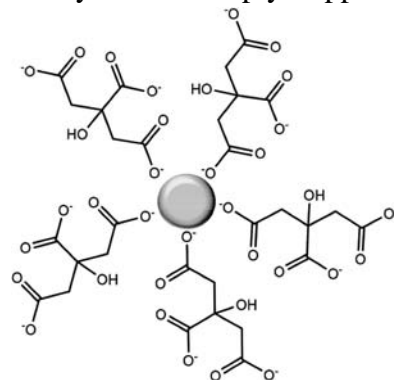


**Figure 5.1** Nanoparticle grafted with citrate groups.

In general, nanoparticles functionalized with positively charged ligands exhibit higher internalization into cells compared to the neutral and negatively charged particles but in some specific applications the negative charge could be more appropriate<sup>46</sup>.

Further investigation should be performed about FITC labeling stability in function of the surrounding's pH and about the effect of these molecules incorporation into nanocomposites.

The final aim of the project indeed could be to study the kinetic of FITC release from the hybrid material under magnetic stimuli, simulating the release of drugs inside human body.

## 5.2 Rheological analysis

The rheological behaviour of the prepared composite materials had been not yet completely defined during this study. Nevertheless, the analysis performed at ultra high oscillation frequencies would be interesting to achieve in order to define the hybrid material behaviour all over the range of frequency, from 0Hz till frequencies in the order of the GHz.

From the tests performed with Brillouin spectroscopy some suggestions can be given for the future analysis; for example, it could be possible trying to prevent particles migration to cell walls, after magnetic field application, using a capillary cell as sample holder since it doesn't let the particles migrate to relatively long distance, away from the optical beam path.

Anyway the next step of rheological analysis rests to perform tests on alginate gel loaded with magnetic NPs. Indeed, during this experience tests were performed only on

composites formed with alginate solution and maghemite NPs, without carrying out the jellification process of such material. Gel consistency is obtained by addition of at least divalent cations to the alginate solution containing the magnetic nanoparticles; generally for alginate jellification calcium  $\text{Ca}^{2+}$  ions are employed, which structure alginate chains in the typical “egg box” configurations (Figure 2.14) where connecting zones are based on weak bonds, thus returning in the irreversibility of the created structure.

Moreover, the material jellification should have to facilitate Brillouin spectroscopy analysis since NPs trapping between the rigid regions of polymer structure should avoid their migration under the magnetic field effect and simplify parameters tuning during the tests.





# Conclusion

As mentioned at the beginning of the thesis, the focus of the study had been to realize a biopolymer based magnetic nano-composite for targeted delivery of drugs in the human body.

A DOPA@Fe<sub>2</sub>O<sub>3</sub> | alginate nanocomposite was produced following an *ex situ* technique in order to finally study its rheological properties under the magnetic field influence.

The nanocomposite's components were produced and analysed separately in order to evaluate various specific characteristics.

First, maghemite NPs were synthesized following the polyol process that in general permit to control NPs size and geometry. TEM and XRD analysis confirmed a narrow size distribution of the synthesized NPs and an average diameter size of about 10nm. XRD results were proper of a magnetic iron oxide and together with powder's colour confirmed maghemite rather than magnetite formation, while TEM images showed a regular spherical geometry for the obtained particles. NPs chemical composition was finally investigated by FTIR spectroscopy that recorded a peak around 690 cm<sup>-1</sup>, generally due to Fe-O bond stretching vibration, which attests the presence of an iron oxide phase.

So-produced NPs were later grafted with DOPA, APTES and PHOSP ligands using proper grafting protocols for each of them. Grafting validation was based on FTIR spectroscopy results, which furnished spectra recording characteristics peaks for each type of decorated NPs. All ligands grafting succeeded and XRD analysis recorded the same peaks of bare maghemite NPs, giving evidence that no phase transformation inside the NPs occurred after grafting process. The effective amount of ligand grafted onto NPs surface was determined by TGA analysis, considering the mass loss recorded in the range of temperatures between 100°C and 600°C; from the results, dopamine grafting seemed to be the less efficient since lower quantity of ligand seemed to be present, but in this case TGA was performed on a smaller sample compared to those used for APTES NPs and PHOSP NPs TGA and maybe results are not completely reliable.

For each type of grafted NPs a study about their stability in function of the pH of the medium containing them was carried out. Solutions with pH ranging from 2 to 13 were prepared with HCl for acid pH and NH<sub>3</sub> for basics in distilled water; then they were used to prepare samples with suspensions of the various grafted NPs and bare NPs in the different pH solution.

ζ-Potential measurement for each of these gave information about the IEP of grafted NPs and their surface charge at physiological pH. It was seen that APTES NPs are those more stable in that pH range because of their higher surface charge (higher ζ-potential) and their

higher IEP (pH $\sim$ 10); also DOPA NPs resulted to be stabilized by dopamine grafting since their IEP was displaced from pH $\sim$ 7, typical of bare NPs, to pH $\sim$ 8; PHOSP NPs, instead, seemed to be the less stable, with an IEP at pH $\sim$ 7.5. Nevertheless as convention, a particle in suspension must have  $\zeta$ -potential values  $> 30\text{mV}$  to be considered stable, but such a value was recorded for none grafted NPs at physiological pH in this study. The higher  $\zeta$ -potential value obtained at pH around 7 was the APTES NPs one equal to about  $20\text{mV}$ , so further study must be carried out to better improve NPs suspension stability.

The following step of the research had been to label such grafted NPs with a fluorophore molecule in order to mimic drug attachment to NPs surface. This is possible since organic fluorophore functionalities and structure is in general similar to those of drugs or protein, with the advantage to adsorb energy in the range of UV-Vis wavelength and thus to be easily observed by optical spectroscopy. The fluorophore molecule chosen for labelling was FITC and the labelling protocol had already been validated in ITODYS laboratories.

The three differently grafted NPs were FITC labelled and then characterized by UV-Vis spectroscopy, determining which of those more efficiently attach drug molecules onto their surface. From spectra observation and data elaboration it was found that the best ligand in FITC bonding was dopamine, with a labelling efficiency of 9.3% against 1.6% calculated for PHOSP NPs and 0.45% found for APTES NPs. The efficiency value obtained for DOPA NPs is in line with maximum efficiency obtained in other study so it can be stated that dopamine is a good ligand for drug attachment at NPs surface.

Considering the overall results of grafted NPs characterization, DOPA NPs seems to be the more suitable compared to APTES NPs and PHOSP NPs for the kind of application considered in this work. Indeed, they have moderately increased their stability in media at physiological pH relative to bare NPs stability in the same conditions and moreover they resulted to be the more efficient in FITC labelling.

For these reasons DOPA NPs were finally chosen to realize the biopolymer-based nanocomposite. The rheological characterization of such material permitted to understand its magnetic structuring and the deriving enhancement of its mechanical properties. Both loss and elastic moduli were found to increase with increasing oscillatory strain frequency and after the application of an external magnetic field; in particular, moduli enhancement was more pronounced at low oscillation frequencies. It was also found that material's structuring-time after magnetic field application is lower for high values of magnetic field. Other tests pointed out that the shear viscosity of the material increases with the magnetic field strength, especially at low shear rate. When the magnetic field was switched-off the material relaxed its structure and it re-organized itself in the same structure after another application of the magnetic field. This result was useful to prove the magnetic reversibility of the material.

Several opportunity of further development can be considered for the presented work.

First of all, it would be interesting to study the stability in physiological media for novel types of properly grafted NPs and then investigate their efficiency in drug attachment. Some ligands that could be taken into account are diazonium salts and citrate. After the preparation of grafted and labelled NPs it would be interesting also studying the stability of the fluorophore-NP bond varying the pH of the surrounding.

Finally the jellification of the produced nanocomposite may lead to a more complete knowledge of the material's behaviour under magnetic stimuli, varying the oscillatory strain frequency up to the order of GHz. Such an investigation, considering FITC labelled NPs as nanocomposite's fillers, may further furnish information about drug release mechanism by application of mechanical or magnetic solicitations.

We hope that after several other investigations, this kind of material may soon pass from the research level to that of a usual material.



# Nomenclature

$A$	=	absorbance
$B$	=	magnetic induction
$d$	=	intercrystalline planes distance
$De$	=	Deborah number
$E$	=	Young modulus
$G$	=	shear modulus
$G^*$	=	complex shear modulus
$G'$	=	storage modulus
$G''$	=	loss modulus
$H$	=	magnetizing field
$I$	=	intensity of transmitted radiation
$I_0$	=	intensity of incident radiation
$l$	=	path length of the absorbing solution
$M$	=	magnetization
$T$	=	transmittance
$\chi$	=	magnetic susceptibility
$\Delta\zeta$	=	zeta potential standard deviation
$\varepsilon$	=	tensile strain or molar extinction coefficient
$\gamma$	=	shear strain
$\dot{\gamma}$	=	shear rate
$\eta$	=	dynamic viscosity
$\lambda$	=	radiation wavelength
$\mu$	=	magnetic permeability
$\nu$	=	wave number
$\sigma$	=	tensile stress
$\tau$	=	shear stress
$\omega$	=	rotational speed
$\zeta$	=	zeta potential

## Acronyms

ATR	=	Attenuated Total Reflectance
APTES	=	3-aminopropyl-triethoxysilane
APTES NPs	=	3-aminopropyl-triethoxysilane grafted nanoparticles
DEG	=	diethylenglycol

DOPA	=	3-hydroxytyramide hydrochloride
DOPA NPs	=	dopamine grafted nanoparticles
DSC	=	differential scanning calorimetry
DTA	=	differential thermal analysis
FC	=	field cooling
FITC	=	fluorescein isothiocyanate
FITC NPs	=	fluorescein grafted nanoparticles
FT-IR	=	Fourier Transform Infra Red spectroscopy
G	=	guluronate
IEP	=	isoelectric point
JCPDS	=	Joint Committee for Powder Diffraction Standard
M	=	mannurate
MNPs	=	magnetic nanoparticles
MRI	=	magnetic resonance imaging
NPs	=	nanoparticles
PEG	=	polyethilenglycol
PHOSP	=	3-aminopropylphosphonic acid
PHOSP NPs	=	3-aminopropylphosphonic acid grafted nanoparticles
TEG	=	tetraethylenglycol
TEM	=	transmission electron microscopy
THF	=	tetrahydrofuran
XRD	=	X-ray diffraction
ZFC	=	zero field cooling
JCPDS	(Joint Comitee for Powder Diffraction Standard)	

# Bibliography

- <sup>1</sup> C. Corot, P. Robert, J.M. Idee, M. Port (2006). *Adv. Drug Delivery Rev.* 58, 1471.
- <sup>2</sup> J.H. Gao, H.W. Gu, B. Xu (2009). *Acc. Chem. Res.* 42, 1097.
- <sup>3</sup> S. Mornet, S. Vasseur, F. Grasset, E. Duguet (2004). *J. Mater. Chem.* 14, 2161.
- <sup>4</sup> Li Z, Tan B, Allix M, Cooper AI, Rosseinsky M J. (2008). *Small* 4, 231.
- <sup>5</sup> López Pérez JA, López Quintela MA, Mira J, Rivas J, Charles SW (1997). *J. Phys. Chem. B* 101, 8045.
- <sup>6</sup> K Park, Y An, J.G. Hwang, H.J. Park, J.Y. Noh, J.H. Kim, N.M. Park, T. Hyeon (2004). *Nat. Mater.* 3, 891.
- <sup>7</sup> Guardia P, Perez N, Labarta A, Batlle X (2010). *Langmuir* 26, 5843.
- <sup>8</sup> Ge S., Shi X., Sun K., Li C., Uher C., Baker Jr. J.R., Banaszak Holl M.M., Orr B.G. (2009). *J. Phys. Chem. C* 113, 13593.
- <sup>9</sup> Dumestre F, Chaudret B, Amiens C, Renaud P, Fejes P. (2004). *Science* 6, 821.
- <sup>10</sup> Ammar S, Helfen A, Jouini N, Fiévet F, Rosenman I, Villain F, Molinié P, Danot M (2001). *J. Mater. Chem.* 11, 186.
- <sup>11</sup> Cai W, Wan J.Q. (2007). *J. Colloid Interface Sci.* 305, 366.
- <sup>12</sup> Ammar S, Jouini N, Fiévet F, Grenèche JM, Danot M, Molinié P (2006). *J. Phys.: Condens. Matter.* 18, 9055.
- <sup>13</sup> A. Zaffaroni (1974). Drug-delivery system, Patent Number: 385448, *United States Patent*.
- <sup>14</sup> S. Davis, L. Illum (1988). Polymeric microspheres as drug carriers, *Biomaterials*, Vol.9, Issue 1, Pages 111-115. Department of Pharmacy, University of Nottingham.
- <sup>15</sup> Ana L. Daniel-da-Silva, T. Trindade. Biofunctional Composites of Polysaccharides Containing Inorganic Nanoparticles. University of Aveiro, Portugal.
- <sup>16</sup> M. Hamidi, A. Azadi, P. Rafiei (2008). Hydrogel nanoparticles in drug delivery. *Advanced Drug Delivery Reviews* 60, 1638–1649.
- <sup>17</sup> N. Kashyap, N. Kumar, M. Kumar, (2005). Hydrogels for pharmaceutical and biomedical applications. *Crit. Rev. Ther. Drug Carr. Syst.* 22, 107–149.
- <sup>18</sup> A.S. Hoffman (2002). Hydrogels for biomedical applications. *Adv. Drug Deliv. Rev.* 43, 3–12.
- <sup>19</sup> N.A. Peppas (Ed.) (1987). Hydrogels in Medicine and Pharmacy. *Synthetic Polymers, vol. I–III*, CRC Press, Boca Raton, FL,.
- <sup>20</sup> S. Venkatesh, M.E. Byrne, N.A. Peppas, J.Z. Hilt (2005). Applications of biomimetic systems in drug delivery. *Expert Opin. Drug Deliv.* 2 (6), 1085–1096.
- <sup>21</sup> N.A. Peppas, A.G. Mikos (1986). Preparation methods and structure of hydrogels. *N.A. Peppas (Ed.), Hydrogels in Medicine and Pharmacy, vol. 1*, 1–27.

- <sup>22</sup> L. Brannon-Peppas (1990). Preparation and characterization of crosslinked hydrophilic networks. *L. Brannon-Peppas, R.S. Harland (Eds.), Absorbent Polymer Technology, Elsevier, Amsterdam*, 45–66.
- <sup>23</sup> J.A. Bouwstra, H.E. Jungiger (1993). *Encyclopaedia of Pharmaceutical Technology*, vol. 7, *Marcel Dekker Inc., New York*, 441.
- <sup>24</sup> H.Arami, K.M. Krishnan (2013). *IEEE Transaction on Magnetics* 49 (7).
- <sup>25</sup> R. Mout, D.F. Moyano et al. (2012). *Chem. Soc. Rev.* 41, 2539-2544.
- <sup>26</sup> F. Torney, B. G. Trewyn, V. S. Lin and K. Wang (2007). *Nat. Nanotechnol.* 2, 295–300.
- <sup>27</sup> L. Ourry (2011). Hydrogels de biopolymères nanocomposites magnéto-sensibles. *Master thesis*. Lab. ITODYS, Université Paris Diderot- Paris 7.
- <sup>28</sup> Fiévet (1989).
- <sup>29</sup> L. Poul, S. Ammad et al. (2000). Metastable solid solution in the system ZnO-CoO: synthesis by hydrolysis in polyol medium and study of the morphological characteristics. *Solid State Sciences* 3, 31-42.
- <sup>30</sup> J. Fouineau (2011). Étude expérimentale et théorique du greffage de ligands organiques à la surface de nanoparticules d'oxyde de fer. *Chemistry master thesis*. Paris Diderot University.
- <sup>31</sup> D. Caruntun, B.L. Cushing, G. Caruntu, C.J. Oconnor (2005). *Chem Mater.* 17, 3398.
- <sup>32</sup> N. Benjamaa (2012). Interfaces, Traitements, Organisation et Dynamique des Systèmes. *Master Thesis*. Université Paris Diderot.
- <sup>33</sup> J.D. Marshall, W.C. Eveland, C.W. Smith (1958). Superiority of Fluorescein Isothiocyanate for Fluorescent-Antibody Technic with a Modification of its Application. *Exp Biol Med (Maywood)* 98, 898-900.
- <sup>34</sup> A. Hanini (2012). Bioeffects of ferrite nanoparticles considered for cancer hyperthermia therapy. *Ph.D Thesis*. University of Paris Diderot and University of Carthage-Tunisia.
- <sup>35</sup> S. Brulé, M. Levy et al. (2011). Doxorubicin release triggered by alginate embedded magnetic heaters: a combined therapy. *Advanced Materials* 23, 787-790.
- <sup>36</sup> S.H. Hu, T.Y. Liu et al. (2007). Controlled Pulsatile Drug Release from a Ferrogel by a High-Frequency Magnetic Field. *Macromolecules* 40, 6786-6788.
- <sup>37</sup> <http://www.fmcbiopolymer.com/>
- <sup>38</sup> R.D. Waldron (1955). *Phys. Rev.* 99, 1727.
- <sup>39</sup> M.A. Gabal, Y.M. Al Angari (2009). *Mater. Chem. Phys.* 115, 578.
- <sup>40</sup> W.B. White, B.A. De Angelise (1967). *Spectrochim. Acta, Part A* 23, 985.
- <sup>41</sup> P.S. Sidhu (1988). Transformation of trace element-substituted maghemite to hematite. *Clays and Clay Minerals* 36, 31-38.
- <sup>42</sup> X.D. Liu, S. Tokura et al. (2002). *Carbohydrate Polymers* 49, 103-108.
- <sup>43</sup> R. Tian, O. Seitz et al. (2010). Infrared Characterization of Interfacial Si-O Bond Formation on Silanized Flat SiO<sub>2</sub>/Si Surfaces. *Langmuir* 26 (7), 4563-4566.



- <sup>43</sup> F.Gazeau, F.Boué et al. (2003). *J. Phys.: Condens. Matter* 15, 1305-1334.
- <sup>44</sup> T.Solkolov, S.Naik. Novel type of fluorescent silica nanoparticles: towards ultrabright silica nanoparticles. Clarkson University.
- <sup>45</sup> E.Rampazzo, S.Bonacchi et al. (2010). *Journal of Physical Chemistry* 114, 45.
- <sup>46</sup> E.C. Cho, J.Xie et al. (2009). *Nano Lett.* 9, 1080–1084.